THESIS FOR THE DEGREE OF LICENTIATE OF ENGINEERING

# Neutron spectroscopy and computational studies of hydride-ion dynamics in oxide- and nitride-hydride materials

Lucas Fine

Department of Chemistry and Chemical Engineering
CHALMERS UNIVERSITY OF TECHNOLOGY
Göteborg, Sweden 2024

**Neutron spectroscopy and computational studies of hydride-ion dynamics in oxide- and nitride-hydride materials**

Lucas Fine



Licentiatuppsatser vid Institutionen för kemi och kemiteknik
Chalmers tekniska högskola.
Nr 2024:04

This thesis work is part of a collaboration agreement between Chalmers University of Technology and the Institut Laue-Langevin (ILL), Grenoble, France. It has been financially supported primarily by grants from the ILL and the Swedish Research Council. I have spent the majority of my time at the ILL.

Department of Chemistry and Chemical Engineering
Chalmers University of Technology
SE-41296 Göteborg, Sweden

Göteborg, Sweden 2024

**Neutron spectroscopy and computational studies of hydride-ion dynamics in oxide- and nitride-hydride materials**

Lucas Fine
Department of Chemistry and Chemical Engineering
Chalmers University of Technology

## Abstract

This thesis presents studies of the hydride-ion dynamics in the nitride- and oxide-hydride materials $Ca_3CrN_3H$ and $BaTiO_{3-x}H_x$ (with $x < 0.2$). These mixed-anion compounds are of great interest because they show capabilities for hydrogen transport and catalysis, but fundamental questions concerning the hydride-ion dynamics in these materials remain to be answered. Here, these questions have been tackled using inelastic and quasielastic neutron scattering techniques, as well as density functional theory calculations.

For $Ca_3CrN_3H$, it is found that hydride-ions undergo one-dimensional diffusion, which supposedly mediated by the presence of vacancies in the hydride-ion sublattice, The measured diffusion coefficient is comparable to the three-dimensional hydride-ion diffusion in $BaTiO_{3-x}H_x$. This result suggests that reducing dimensionality might be used to optimize the hydride-ion diffusivity in oxide- and nitride-hydride materials. In addition, it was demonstrated that hydride-ion vacancies are present in the material, which impact the vibrational frequencies of hydride-ions and thus their jump rate. This implies that the hydride-ion diffusivity may be tailored by tuning the hydride-ion vacancy.

For $BaTiO_{3-x}H_x$, the results corroborated earlier findings which showed that hydride-ion diffusion relies on the presence of oxygen vacancies serving as jumping sites for the hydride-ions. Specifically, two time scales of diffusion were observed, indicating significant inhomogeneity in the local diffusion environment of the hydride-ions. This new finding suggests that understanding and controlling these inhomogeneities may be used to optimize the hydride-ion diffusivity. Finally, it was found that the presence of valence electrons localised near the hydride-ion–oxygen vacancy pair hinders the jump diffusion mechanism, indicating a correlation of electronic and ionic mobility in $BaTiO_{3-x}H_x$. This implies that tuning the hydride-ion conductivity will impact the electronic conductivity of the material, an effect which should be considered for technological applications of $BaTiO_{3-x}H_x$ such as its use in fuel cells.

**Keywords**: *Oxide-hydride, nitride-hydride, hydride-ions, quasielastic neutron scattering, diffusion, inelastic neutron scattering, phonons, density functional theory.*

# List of publications

This thesis is based on the following publications:

**I** **One-dimensional hydride-ion diffusion in the nitride-hydride $Ca_3CrN_3H$** L. Fine, R. Lavén, W. Zefeng, Y. Cao, T. Tsumori, M. Matsuura, H. Tamatsukuri, H. Kageyama, M. M. Koza, and M Karlsson
*In Manuscript*

**II** **Local structure and vibrational dynamics in the nitride-hydride $Ca_3CrN_3H$** L. Fine, R. Lavén, W. Zefeng, Y. Cao, T. Tsumori, R Kajimoto, M Jimenéz-Ruiz, H. Kageyama, M. M. Koza, and M Karlsson
*In Manuscript*

**III** **Hydride diffusion in oxyhydride barium titanate: insights from incoherent quasielastic neutron scattering** R. Lavén, L. Fine, H. Guo, U. Häussermann, M. Matsuura, M. M. Koza, and M. Karlsson
*In Manuscript*

**IV** **Coupled migration of electronic defects and hydride-ions in the oxygen-deficient oxyhydride barium titanate** L. Fine, I. Panas, M Karlsson, and M. M. Koza
*In Manuscript*

# Contribution report

My contributions to the included papers:

**I** I contributed to the planning of the QENS experiment, I was co-responsible for the data collection and main responsible for the data analysis. I was the main responsible for writing the manuscript.

**II** I contributed to the planning of the INS experiments, I was the main responsible for the data collection and the data analysis. I was the main responsible for the planning, the realisation, and the data analysis of the DFT calculations. I was the main responsible for writing the manuscript.

**III** I contributed to the planning of one of the QENS experiments, for which I was the main responsible for the data collection and the data analysis. I contributed to the writing of the result section of the manuscript.

**IV** I contributed to the planing of the DFT calculations and I was the main responsible for their realisation and for the data analysis. I was the main responsible for writing the manuscript.

# Contents

# List of abbreviations

| | |
|---|---|
| DFT | Density functional theory |
| DINS | Deep inelastic neutron scattering |
| DOS | Density of states |
| EISF | Elastic incoherent structure factor |
| FWHM | Full-width at half-maximum |
| GDOS | Generalized vibrational density of state |
| ILL | Institut Laue-Langevin |
| INS | Inelastic neutron scattering |
| J-PARC | Japan Proton Accelerator Research Complex |
| QENS | Quasielastic neutron scattering |
| ToF | Time-of-flight |
| XRD | X-ray diffraction |

# Chapter 1

# Introduction

Hydrogen plays a key role in the transition to a decarbonised economy because it is currently employed in many chemical industries and seen as a sustainable energy carrier. However, in 2022, hydrogen constituted less than 2% of the total energy consumption in Europe, and 96% of this hydrogen was generated from natural gas, leading to large $CO_2$ emissions [1, 2]. For example, ammonia ($NH_3$) is seen as a promising hydrogen-based energy carrier [3] and is used as a precursor for fertilizers which are indispensable for the global food production system. However, its production is highly energy consuming,[1] and requires hydrogen gas (involved in the reaction $N_2 + 3H_2 \rightarrow 2NH_3$) which currently relies on highly $CO_2$ emmissive fossil fuel solutions.[2] Over the last decades, there has been an increasing research effort aiming to develop new materials which are more efficient in producing hydrogen (including $H_2$ and $NH_3$ production). The most promising materials for this purpose are often crystalline, but often fundamental questions regarding their hydrogen dynamics remain to be elucidated [7–9]. *Dynamics* in this context refers to motions of various nature, such as vibrations of atoms around an equilibrium position and their diffusion over long ranges (up to a few nanometers), which may lead to macroscopic hydrogen transport and be useful for various applications [7].

Hydrogen ions stand naturally as good charge carrier candidates for designing hydrogen conductors materials because of their small size and lightness, making them highly mobile in many crystalline systems [10–14]. The typical materials of interest are perovskite oxides incorporating hydrogen. In most of these systems, hydrogen is present as protonic ($H^+$) species [10, 15] but hydrogen can be also present as

[1] Representing about 2% of the global energy consumption in 2021 [4].

[2] Steam methane reforming, producing the $H_2$ reactant gas required for $NH_3$ production, releases about 10 tonnes of $CO_2$ equivalent per tonne of $H_2$ formed [5, 6].

hydride-ions ($H^-$), thus forming, so called, oxide-hydrides.

Hydride-ion mobility could be employed in electrolyser and fuel cell technologies, that are used to split water molecules to produce $H_2$ and consume $H_2$ to produce electricity, respectively. Today, there is a need for novel materials to make the current devices more economically and energetically efficient [16]. For example, solid oxide fuel cells suffer from high operating temperatures (usually between 600 and 1000 °C) required by their ion conducting electrolytes. These devices would benefit from new intermediate-temperature (from 450 to 650 °C) solid-state hydride-ion conductors [17, 18]. Hydride-ion mobility is also a feature of interest for the ammonia synthesis reaction ($N_2 + 3H_2 \rightarrow 2NH_3$), which involves hydrogenation of $N_2$ molecules. This reaction requires a catalyst to break the strong $N \equiv N$ triple bond, and oxide-hydrides, as well as nitride-hydrides, i.e., nitride materials incorporating hydride-ions, demonstrated good performances for ammonia synthesis [19–21]. When oxide-hydrides and nitride-hydrides are used as a substrate for ruthenium (Ru) and iron (Fe) nanoparticles, the mobility and the reduction potential of the lattice hydride-ions are determinant for the catalytic activity. While the hydride-ion mobility prevents hydrogen poisoning at the nanoparticle surface, i.e. excessive hydrogen adsorption at the surface preventing a sufficient nitrogen adsorption [Figure 1.1(a)], the hydride-ion reduction potential facilitates the $N_2$ cleavage [Figure 1.1(b)]. Interestingly, in the nitride-hydride material $Ca_3CrN_3H$, exhibiting good catalytic performances without the use of Ru/Fe nanoparticles, a similar mechanism is suspected to take place. Specifically, hydrogenation of the nitrogen gas adsorbed at its surface is believed to be achieved with mobile lattice hydride-ions instead of the hydrogen reactant gas [21, 23]. However, this assumption is based on calculations, and a good understanding of the hydride-ion mobility in the material lacks experimental verification.

Motivated by the background given above, this thesis focuses on investigations of the local structure and the hydride-ion dynamics in two mixed-anion compounds, the oxide- and nitride-hydride materials $Ca_3CrN_3H$ and $BaTiO_{3-x}H_x$. The questions tackled are:

- What are the requirements for hydride-ions diffusion in the bulk $Ca_3CrN_3H$ and $BaTiO_{3-x}H_x$?
- What are the underlying mechanisms?
- How can we enhance the hydride-ion diffusivity?

Answering these questions has a fundamental interest, but has also technological implications, and may be useful for the design of new hydride-ion conductors and

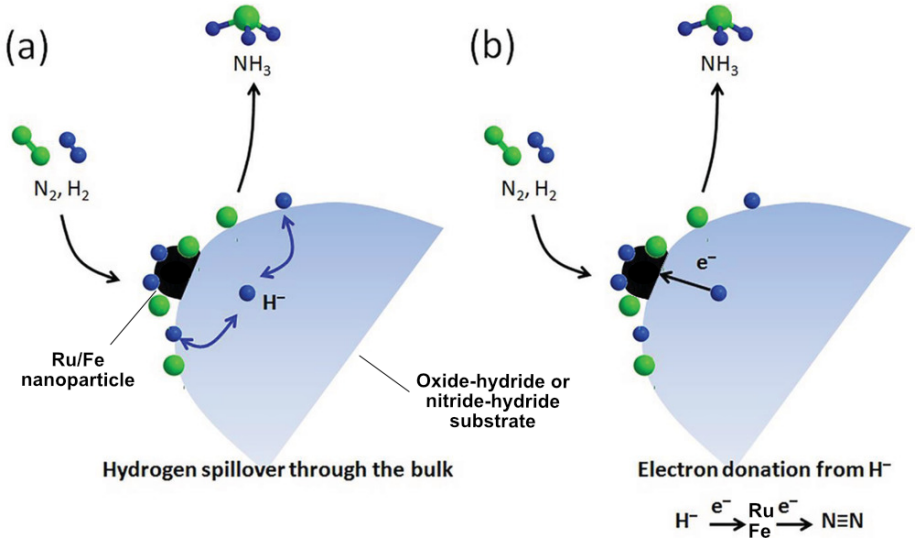


Figure 1.1: Illustration of the ammonia synthesis catalytic mechanism by ruthenium (Ru) and iron (Fe) nanoparticles deposited on oxide-hydrides and nitride-hydrides substrates. (a) The hydride-ion absorption in the substrate prevents hydrogen poisoning at the nanoparticle surface. (b) Electron donation from the hydride-ion to the nanoparticle, assisting in $N_2$ activation. Reproduced with permission from [22]. Copyright 2018 John Wiley and Sons.

catalysts with better efficiencies and operating at lower temperatures.

For that purpose, I used neutron spectroscopy techniques, namely quasielastic and inelastic neutron scattering (QENS and INS), and atomistic computer simulations, namely density functional theory (DFT) techniques.

# Chapter 2

# Mixed-anion compounds

Mixed-anion materials include several anionic species in a single phase, and most explored materials are oxide-based mixed-anions compounds. They include oxide-fluorides, oxide-nitrides, oxide-chalcogenides, oxide-pnictides, and oxide-hydrides, representing less than 3000 available materials, a relatively low number compared to the $\sim$ 52000 known oxide materials [24, 25]. Mixed-anion compounds are characterized by a heterogeneous coordination environment surrounding the cations, a feature not present in conventional single-anion compounds (Figure 2.1). Because of the different chemical characteristics of each anion, such as the polarizability, the valence electron shell, or the ionic radius, fine functionality tuning can be achieved by mixing anions within the same material. For example, replacing oxide-ions with anions of lower electronegativity in a semiconductor material generally reduces the band gap. This strategy was used to enhance the photocatalytic activity for water oxidation in TaON [26], and to design the first water splitting photocatalyst under visible light, a solid solution of GaN and ZnO [27]. Band gap control was also used to tune the color of solid solutions of $CaTaO_2N$ and $LaTaON_2$, and propose non-toxic inorganic pigments [28]. Controlling the dimensionality by stacking layers of different anions is another strategy, which was successfully used to design superconductor materials with a high superconducting transition temperature ($T_c$). These include layered oxide-pnictide materials with the ZrCuSiAs-type structures [29], such as $LaO_{1-x}F_xFeAs$ ($x = 0.05, 0.11$) with $T_c = 43$ K [30] or $SmO_{0.85}FeAs$ with $T_c = 55$ K [31]. In these layered materials, superconductivity arises from the two-dimensional (2D) electronic states caused by the different binding energy of the multiple anions with the cations. This was first demonstrated in the layered oxide-halide $Sr_2CuO_2F_{2+\delta}$, exhibiting $T_c = 46$ K, in which there is a strong covalency between the Cu and O species, while the bonding between Cu and F is ionic [32].

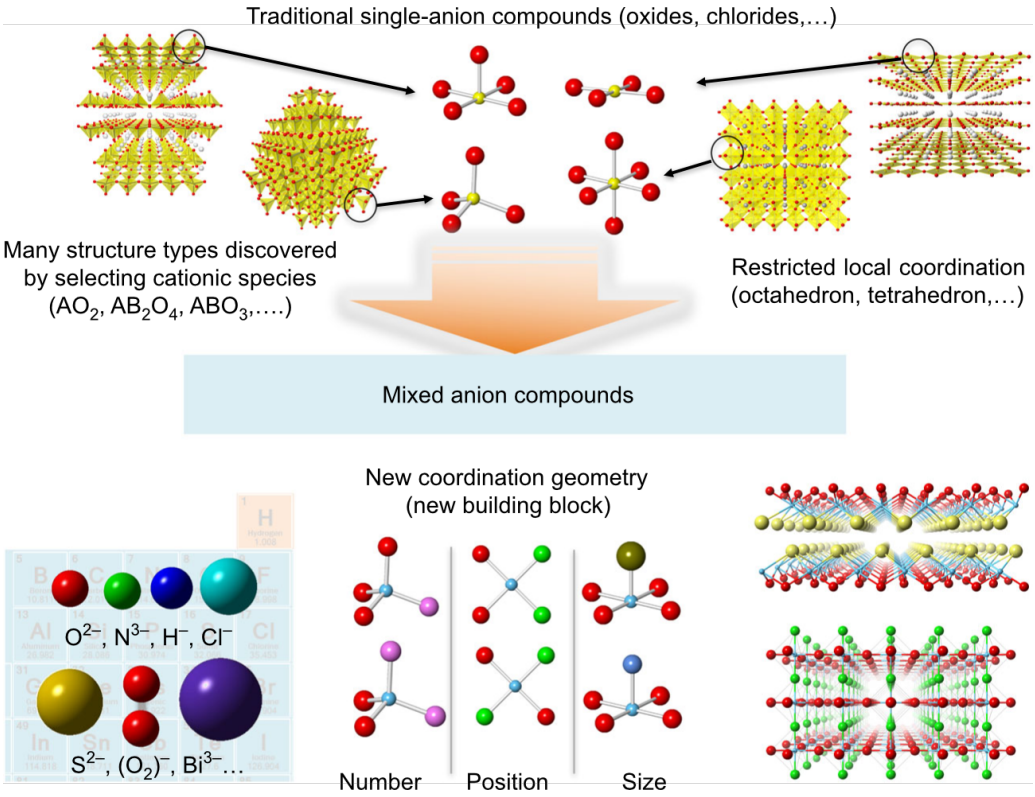


Figure 2.1: Illustration of the new possible combination of elements allowed in mixed-anion materials. Reproduced from [24], in open access.

Lowering the cation–anion binding energy is also a strategy to promote conductivity of light ions with low ionic charge. This strategy was used by doping the Cl-ion conductor LaOCl with calcium, resulting in $La_{1-x}Ca_xOCl_{1-x}$ ($x = 0.05 - -.4$), with a three orders of magnitude greater conductivity [33].

In particular, mixed-anion materials including hydride-ions ($H^-$) attracted a lot of interest during the last decade thanks to the new chemistry offered by these materials [34]. Hydride-ions are very flexible in size and therefore can be accommodated in many anionic sites and become easily mobile [35]. Moreover, since hydrogen easily gives or takes up a charge, hydride-ions can turn to protonic species ($H^+$), increasing their adaptability to the local environment. Hydride-ion mobility was observed in several oxide-hydride materials, such as $LaSrCoO_3H_{0.7}$ [36], $SrVO_2H$ [14], $BaTiO_{3-x}H_x$ ($x < 0.6$) [37, 38], and $La_2LiHO_3$, which allowed to use this latter material as electrolyte in a solid-state battery [39]. Another feature of hydride-ions is their valence electron shell, which involves only a 1s orbital and blocks $\pi$-bonding

when positioned between two neighbouring transition metals. This is the case in $SrCrO_2H$, demonstrating the highest antiferromagnetic ordering temperature among chromium oxides [40], or in $SrVO_2H$, showing a pressure-induced insulator-to-metal phase transition [41].

This thesis focuses on investigations of two specific types of mixed-anion materials, namely the oxide-hydride $ATiO_{3-x}H_x$ (A = Ba, Sr, and Ca, $x < 0.6$) and the nitride-hydride $Ca_3CrN_3H$. These materials are described in the following section.

## 2.1 The oxide-hydride $ATiO_{3-x}H_x$

### 2.1.1 Structural properties

Materials of stoichiometry $ATiO_{3-x}H_x$ (A = Ba, Sr, and Ca, $x < 0.6$) belong to the wider class of transition metal oxide-hydrides, for which the interest began with $LaSrCoO_3H_{0.7}$, discovered in 2002 by Hayward *et al.* [42]. They showed that the hydride-ions have a role in mediating magnetic exchange interactions and have a complex bonding character with other species [43]. Further experiments demonstrated that hydride-ions are also mobile in this structure [36], opening the way for hydride-ion transport chemistry with transition metal oxide-hydrides.

$ATiO_{3-x}H_x$ (A = Ba, Sr, and Ca, $x < 0.6$) have a pervoskite structure close to their parent oxide, $ATiO_3$, which consist of a cubic, tetragonal, or orthorhombic lattice of A cations, hosting a sublattice of corner-sharing $TiO_6$ octahedra. In the oxide-hydride phase, some $O^{2-}$ are replaced by stochastically distributed $H^-$ (Figure 2.2). $BaTiO_{3-x}H_x$, with $x < 0.6$, was first synthesized by Kobayashi *et al.* in 2012

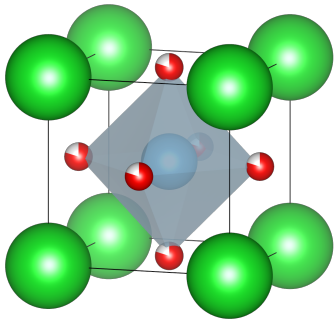

Figure 2.2: Cubic crystal structure of $BaTiO_{3-x}H_x$, $x < 0.6$. Ba, Ti, O and H are represented by green, blue, red, and white spheres. The red and white spheres indicate that the site can be occupied either by an oxygen or an hydrogen species.

*via* a topochemical reaction of $CaH_2$ with the parent oxide $BaTiO_3$ [37]. This finding was quickly followed by the discovery of $CaTiO_{3-x}H_x$ and $SrTiO_{3-x}H_x$, as well as solid solutions of $(Ba, Sr, Ca)TiO_{3-x}H_x$, *via* a similar topochemical synthesis route [44, 45]. Topochemical means that the product is formed in a limited number of reaction steps, involving only the bond breaking and bond forming necessary to the exchange of O and H atoms. This mechanism explains why the oxide and the oxide-hydride phase have similar crystal structures. At room temperature, both $CaTiO_3$ and $CaTiO_{3-x}H_x$ are orthorhombic ($Pnma$), and both $SrTiO_3$ and $SrTiO_{3-x}H_x$ are cubic ($Pm\overline{3}m$). However, $BaTiO_3$ is tetragonal ($P4mm$) whereas $BaTiO_{3-x}H_x$ is cubic ($Pm\overline{3}m$). This change is due to a reduction of the Ti(4+) species to Ti(3+) which cancels the ferroelectric distortion, i.e. the small off-centering of the Ti atom along a crystallographic axis, causing the tertragonal symmetry [44]. Conversely, $CaTiO_3$ and $SrTiO_3$ are not ferroelectric and their orthorhombic structure is due to a tilt of the $TiO_6$ octahedra, which is barely affected by the reduction of Ti(4+/3+)[44].

### 2.1.2 Hydride-ion mobility

The first indication that the hydride-ions can be mobile in $ATiO_{3-x}H_x$ (A = Ba, Sr, and Ca, $x < 0.6$) came from thermal gravimetric analysis/mass spectrometry (TGA-MS) experiments. When heated under inert atmospheres, the pure phases and solid solutions of $(Ba, Sr, Ca)TiO_{3-x}H_x$ released hydrogen as $H_2$ gas at temperatures between 400 °C and 500 °C [44] (Figure 2.3). When heated under air, $BaTiO_{3-x}H_x$ released $H_2$ around 200 °C and absorbed $O_2$ from the environment to reform the parent oxide $BaTiO_3$ [37]. In addition, the hydride-ions were also found exchangeable with deuterium ions in thin films of $SrTiO_{3-x}H_x$ and powder samples of $BaTiO_{3-x}H_x$. In both cases, the authors suggested that the hydride-ion diffusion mechanisms rely on the presence of vacancies in the O/H sublattice, leaving space for the formation of percolation pathways in the perovskite lattice [37, 38, 45–48].

Tang *et al.* conducted systematic H/D exchange and $H_2$ release experiments on a series of $BaTiO_{3-x}H_x$ ($0.35 < x < 0.60$) samples [48] [Figure 2.4(a)]. The kinetics analysis yielded activation energies in the range of 2.1–3.8 eV, with a decreasing tendency with increasing x. Because all the anionic sites are expected to be occupied by either $O^{2-}$ or $H^-$, it was assumed that the percolation of hydride-ions begins with the creation of an initial vacancy at the surface of the material. This vacancy can then diffuse in the bulk with consecutive migrations of $O^{2-}$ or $H^-$. The correlation between the activation energy and the hydride-ion concentration is interpreted as a consequence of the migration of $O^{2-}$. Because the activation energy of $O^{2-}$ in similar materials is close to the highest values in this study, the authors suggested that for

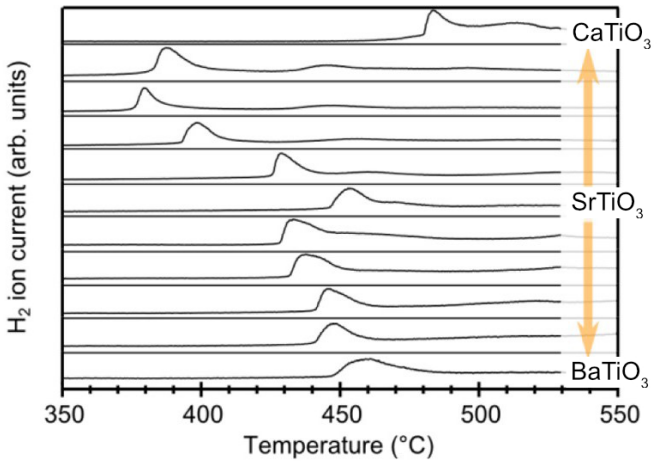


Figure 2.3: $H_2$ gas release temperature from $(Ba, Sr, Ca)TiO_{3-x}H_x$ compositions during heating. From top to bottom, the final products $Sr_yCa_{1-y}TiO_{3-y}$ (y = 0, 0.2, 0.4, 0.6, 0.8, 1.0) and $Sr_{1-y}Ba_yTiO_{3-y}$ (y = 0.2, 0.4, 0.6, 0.8, 1.0). Reproduced with permission from [44]. Copyright 2012 American Chemical Society.

$x < 0.4$, the hydride-ion diffusion is limited by the oxide ion diffusion. For $x > 0.4$, the activation energy decreases, which was interpreted as diffusion of hydride-ions exclusively. In addition, they suggested that the migration mechanism for $O^{2-}$ and $H^-$ consists of jumps between nearest-neighbor (NN) sites or next-nearest-neighbor (2NN) sites in the anion lattice. As each anionic site possesses 8 nearest neighbor (NN) sites, a minimum occupancy of 25% by hydride-ions is required (corresponding to $x > 0.75$) within the anion lattice to establish neighboring chains of hydride ions. Because such a high hydride-ion content was not achieved experimentally, it was concluded that for $0.4 > x > 0.75$, the diffusion must include both NN and 2NN jumps, while for $x < 0.4$, it should consists of NN jumps only.

In the mechanism proposed above, anion vacancies are created at the surface with an initial hydrogen release during the experiment. However, it was later found that the presence of a non-negligible amount of vacancies can be obtained already at the reduction stage of the parent oxide, by tuning the reaction conditions [49, 50]. In a first study, Nedumkandathil *et al.* were able to synthesise the stoichiometries $BaTiO_{3-x}H_y\square_{x-y}$ with x up to 0.6 and y in the range of 0.04–0.25 by varying the metal-hydride serving as reducing agent [50]. Later on, they obtained $BaTiO_{2.9-x}H_{0.1}\square_x$ with x up to 0.4 by varying the synthesis temperature [49].

Consequently, it was evident to investigate the hydride-ion diffusion mechanism in samples including vacancies, namely $BaTiO_{3-x}H_y\square_{x-y}$. In $LaSrCoO_3H_{0.7}$, the

diffusion mechanism is also believed to consist of hopping motions of hydride-ions between vacant sites [36]. This conclusion was made on the basis of the analysis of QENS data. Following this idea, Eklöf-Österberg *et al.* conducted in 2019 a first QENS experiment on $BaTiO_{3-x}H_y\square_{x-y}$ with x in the range of 0.18–0.7 and y in the range of 0.04–0.1 [13]. Interestingly, the analysis of the data showed that hydride-ions are diffuse already at ambient temperature (300 K), with a jump distance between 2.7 and 5.2 Å, with an increasing trend with increasing temperature. This was interpreted in terms of NN and 2NN jumps. At 250 K and below, the hydride-ions were found to jump between NN sites, with a separation of 2.5 Å, while above 400 K, they were found to also jump between 2NN sites, with a separation of 4 Å [Figure 2.4(b)]. However, these results need consolidation and motivate further QENS measurements. In addition to the proposition of a diffusion mechanism for $H^-$, the study estimated an activation energy of about 100 meV. This relatively low value explains why diffusion is already observed at room temperature. Similarly, a value for the diffusion coefficient could also be extracted from the QENS data, and was found to be in the range of $10^{-5}$ $cm^2s^{-1}$ above 300 K and $10^{-6}$ $cm^2s^{-1}$ below.

Interestingly, all the aforementioned studies [13, 48] propose the same migration mechanism but report activation energies differing by more than 10 orders of magnitude, i.e $E_a \sim 0.1$ eV in [13] and $E_a \sim 2$ eV in [48]. This variance in $E_a$ may be linked to differences in oxygen vacancy concentrations. Moreover, the H/D exchange experiment can be hampered by surface and grain boundary effects, whereas QENS probes the bulk self-diffusion of hydride-ions, i.e. between grain boundaries. Consequently, the results from these experiments must be compared with care.

The hydride-ion migration mechanism was also investigated with computational techniques. Tang *et al.* used DFT to estimate the energy barrier that $H^-$ must overpass to jump between NN sites or between 2NN sites [48]. They showed that the barrier in the second process is about 3 times higher than in the first. This qualitatively agrees with the experimental observation with QENS of NN jumps at low temperature and 2NN at higher temperatures. The calculated activation energies are $\sim 1$ eV and $\sim 3$ eV, which is in the order of magnitude of the results from the H/D exchange experiments, but much larger than the QENS value of $\sim 100$ meV. Another computational study, conducted by Liu *et al.* [51], obtained an energy barrier of 0.28 meV for the NN jumps, a value closer to the QENS data. These experimental and computational results are summarized in Table A.1. In summary, a remaining open question concerning this material is:

- What is the origin of the discrepancies between experimental and theoretical results on hydride-ion diffusion in $BaTiO_{3-x}H_x$?

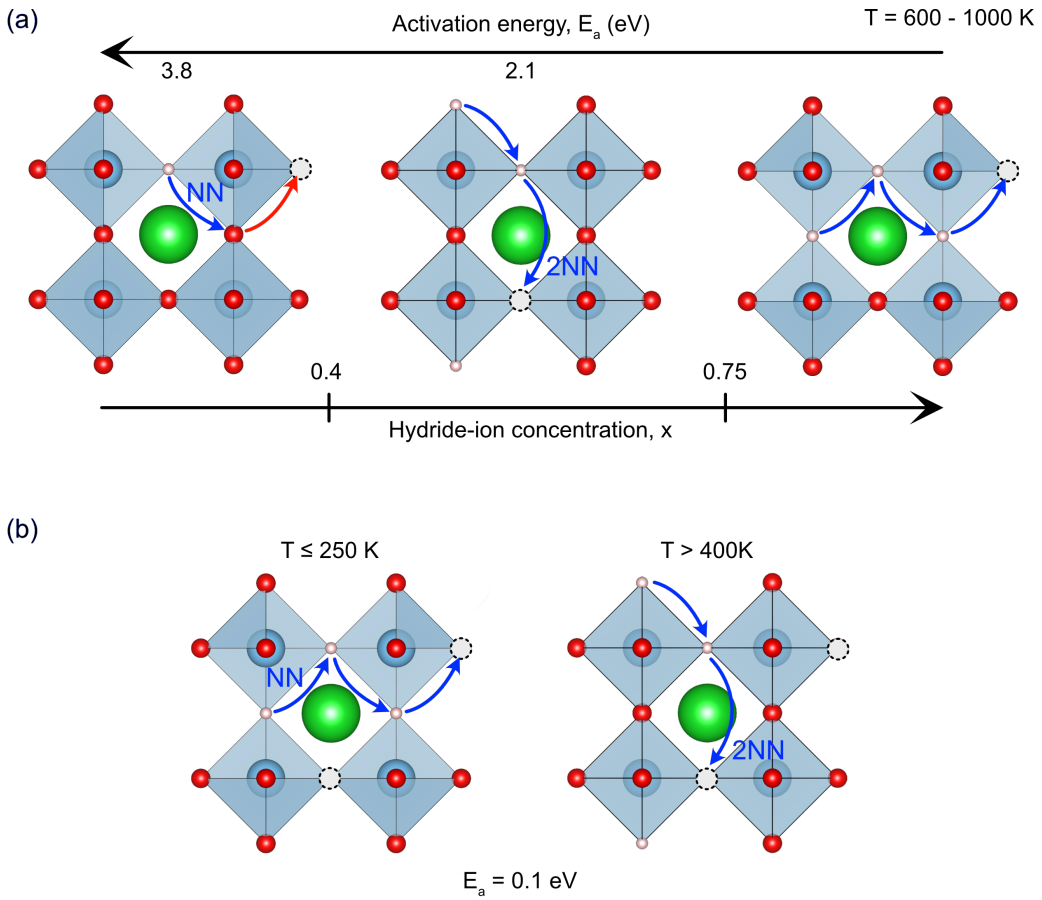


Figure 2.4: Hydride-ion jump diffusion mechanism in $BaTiO_{3-x}H_x$ as proposed in (a) ref. [48] and (b) ref. [13].

### 2.1.3 Electronic properties

Despite the insulator character of the parent oxides $ATiO_3$ (A = Ba, Sr, and Ca), showing band gaps in the range of 3.1–3.5 eV [52, 53], powder samples and thin films of $ATiO_{3-x}H_x$ (A = Ba, Sr, and Ca, $x < 0.6$) exhibit electronic conductivity [37, 45]. This is due to the incorporation of hydride-ions, reducing the oxidation state of titanium ions from +4 to +(4-x) [54, 55].

Measurements of the electrical resistivity showed a semiconductor behavior in pelletized powder samples of $BaTiO_{3-x}H_x$, with x up to 0.6 [37]. On the other hand, thin films of $ATiO_{3-x}H_x$ (A = Ba, Sr, and Ca, $x < 0.6$), with A = Ba, Sr, and Ca, showed a conductor behavior [45]. To investigate the effect of the doping level on

the conductor behavior, Bouilly *et al.* conducted a systematic study on thin films of $BaTiO_{3-x}H_x$ and $SrTiO_{3-x}H_x$ with x between 0.05 and 0.6 [56]. They found that, at room temperature, $SrTiO_{3-x}H_x$ is electrically conducting over the entire range of x values, while $BaTiO_{3-x}H_x$ is a semiconductor for $x < 0.2$ and a conductor for $x > 0.2$. To explain these results, it is speculated that a slight off-centering of the $Ti^{4+}$ ions from their ideal position in the center of the $Ti(O/H)_6$ octahedra localises the doping electrons around the displaced Ti, creating in-gap electronic states and resulting in a semiconductor behavior. Such a local lattice distortion associated with a localised electron is called a *polaron*. In this speculation, polarons should be absent in $SrTiO_{3-x}H_x$ and $BaTiO_{3-x}H_x$ with $x > 0.2$, in which the doping electrons are expected to be equally distributed over all Ti atoms and occupy states in the conduction band.

Following this study, the existence of polarons in $BaTiO_{3-x}H_x$ was tested by Granhed *et al. via* DFT and INS [57] (Figure 2.5). They compared the experimental vibrational spectrum of hydride-ions with the theoretical spectrum in presence and absence of polarons, and concluded that doping electrons in $BaTiO_{3-x}H_x$ tend to occupy the conduction band rather than polaronic states. Consequently, the semiconducting behavior observed in powder samples of $BaTiO_{3-x}H_x$ might be an effect of grain boundaries and might not reflect the bulk conductivity. However, Granhed *et al.* carried out their calculations in a fully stoichiometric model of $BaTiO_{3-x}H_x$, i.e. free of oxygen vacancies. As a result, a natural remaining open question is:

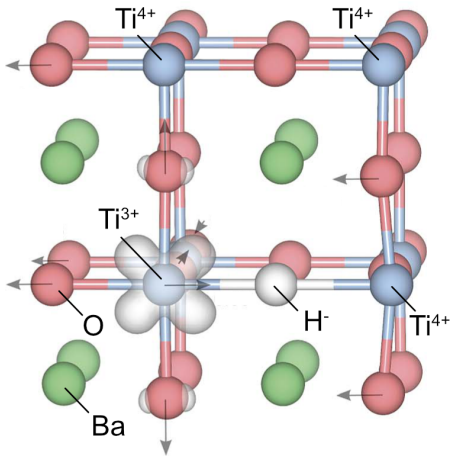


Figure 2.5: Polaron state of $BaTiO_{3-x}H_x$. The white isosurface shows the electron density of the polaron. The arrows represent the local lattice distortion associated with the polaron. Adapted from [57], in open access.

- Do polarons exist in non-stoichiometric composition of $BaTiO_{3-x}H_x$, i.e including oxygen vacancies, and what is their impact on the electronic and ionic conductivity of the material?

## 2.2 The nitride-hydride $Ca_3CrN_3H$

### 2.2.1 Crystal structure

$Ca_3CrN_3H$ was synthesized for the first time in 2022 by Cao *et al.* *via* a topochemical route [23]. They exposed the parent nitride $Ca_3CrN_3$ to $H_2$ gas at 400 °C and obtained the nitride-hydride phase $Ca_3CrN_3H$. It demonstrated an efficient catalytic activity for ammonia synthesis, promoted by a facile mobility of hydrogen species in the bulk of the material [21].

$Ca_3CrN_3H$ is hexagonal, of space group $P6_3/m$. It can be described as an antiperovskite of stoichiometry $X_3BA$ where X = $Ca^{2+}$, B = $H^-$, and A = $[CrN_3]^{5-}$. The Ca ions form $HCa_6$ octahedra which share one face with each other, resulting in unidirectional channels along the crystallographic *c*-axis. The hydride-ions are hosted within the channels, and are lying in the center of each octahedra. The $[CrN_3]^{5-}$ units consist of triangular planar moieties separating the Ca channels in the *ab*-plane (Figure 2.6). $Ca_3CrN_3H$ is stable under inert atmosphere up to approximately 400 °C. Above this temperature, it releases $H_2$ gas. Interestingly, the compound retains its hexagonal structure after de-hydrogenation, while the parent nitride, $Ca_3CrN_3$, is orthorhombic before hydrogenation. This observation indicates that the meta-stable

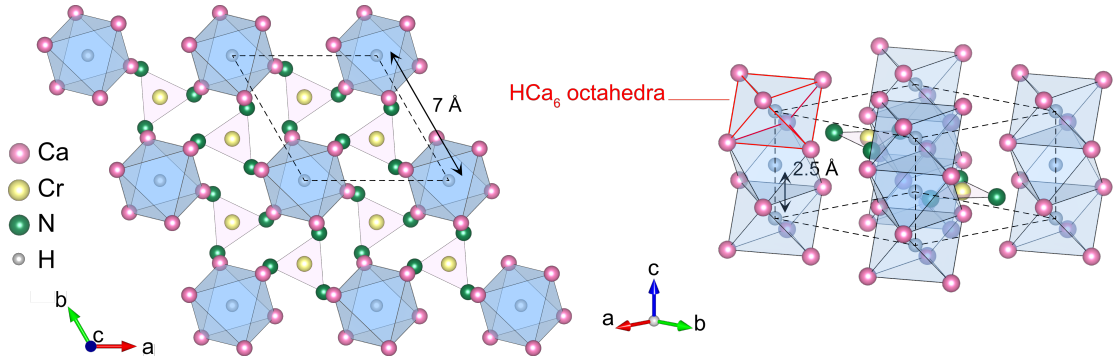


Figure 2.6: Crystal structure of $Ca_3CrN_3H$. The dotted line delimits a unit cell. Reproduced with permission from [23]. Copyright 2022 John Wiley and Sons.

phase of hexagonal $Ca_3CrN_3$ is robust. When the later is exposed back to $H_2$ gas at 400 ℃, it returns to $Ca_3CrN_3H$ [23].

Despite the good knowledge of the average structure of $Ca_3CrN_3H$, as determined from X-ray diffraction (XRD), the local structure surrounding hydride-ions remains unclear because of the poor sensitivity of X-rays to hydrogen species. More specifically, the exact hydride-ion stoichiometry is suspected to be less than one, but between 0.7 and 0.9. This hypothesis is based on mass spectrometry analysis during hydrogen desorption [23]. Consequently, a remaining open question concerning this material is:

- What is the local structure around hydride-ions in $Ca_3CrN_3H$, and does it include hydride-ion vacancies?

### 2.2.2 Hydride-ion mobility

The sorption and desorption properties of $Ca_3CrN_3H$ mentioned above gave the first indication of a facile H diffusion in the material. To investigate this property, transient kinetic analysis experiments were conducted under $H_2/D_2$ gas [23]. It was observed that when a sample of $Ca_3CrN_3H$ is exposed to $D_2$ at 400 ℃, it releases HD gas, which demonstrates that $H^-$ is exchangeable with $D^-$. During this experiment, 60% of the hydride-ions were found replaced by deuterium ions, indicating that bulk hydride-ions, and not only surface hydride-ions, are implied in the turnover. In fact, the facile diffusion of the bulk hydride-ions up to the surface is suspected to be an important feature for the catalytic activity of $Ca_3CrN_3H$ in ammonia synthesis (Appendix B) [21]. However, this hypothesis is established on the basis of DFT calculations and would require experimental support. In summary, a remaining open question is:

- What is the hydride-ion diffusion mechanism in $Ca_3CrN_3H$, and how is it affected by temperature and vacancy concentration?

# Chapter 3

# Neutron scattering

This chapter gives a short introduction to neutron scattering theory and techniques. It describes the specific cases of INS and QENS, which have been used in this thesis.[1]

## 3.1 General aspects of neutron scattering

### 3.1.1 About neutrons

Neutron are quantum particles and are characterized by, among others features, a mass, a momentum, a kinetic energy, a wavelength and a frequency. Neutrons wavelengths typically used in scattering techniques are in the order of 1–10 Å. The larger wavelengths correspond to the slowest, less energetic neutrons, called *cold neutrons* [2]. Wavelengths of $\sim 2$ Å correspond to *thermal neutrons*.[3] The smaller wavelengths correspond to faster, more energetic neutrons, called *hot neutrons*.[4] Fortunately, this range of wavelengths matches the typical inter-atomic distance in condensed matter and consequently, when neutron waves are scattered by atoms, their phases create positive and negative interference leading to *Bragg peaks*, reflecting the crystal structure. This phenomenon is called diffraction and can be measured to investigate the atomic arrangement, i.e. the structure, of materials. Moreover, their typical kinetic energy matches the typical thermal excitation energy of atoms in condensed matter. Consequently, neutrons can excite or absorb excitations in the sample, thus losing

[1] The provided formalism is mainly based on the textbook references [58, 59].

[2] Cold neutrons have a typical kinetic energies in the range of $0 - 26$ meV.

[3] A thermal neutron is a neutron in equilibrium with a thermal bath at room temperature, $T = 300$ K. It has a kinetic energy of $E \approx k_B T \approx 26$ meV.

[4] Hot neutrons have a typical kinetic energies in the range of $26 - 500$ meV.

or gaining kinetic energy. The energy exchange can be measured, allowing for the investigation of dynamics of the sample. This technique is known as as neutron spectroscopy and is introduced in more details below.

Another useful property of neutrons is their charge neutrality. Because they carry no electric charge, neutrons do not interact with electron clouds and can therefore penetrate relatively deep into matter (typically a few cm). They interact with nuclei *via* nuclear forces and thus probe the bulk properties of a sample in a non-destructive manner. Comparatively, X-rays, which interact with electrons, typically penetrate a much shorter distance, of $10^{-2}$ to $10^{-5}$ cm when shone onto a sample.

Neutrons carry a magnetic dipole moment and can thus interact with magnetic sources such as the electron magnetic dipole moment. Using this property, the structural arrangement of the magnetic sources in the sample and their dynamics can be observed with neutron scattering. Magnetic scattering was not used in this thesis and will not be discussed further.

Finally, neutrons have a spin angular momentum of $\pm\frac{1}{2}\hbar$ whose orientation may be flipped during the scattering process ($+\frac{1}{2}\hbar \rightarrow -\frac{1}{2}\hbar$ or $-\frac{1}{2}\hbar \rightarrow +\frac{1}{2}\hbar$), and may provide information about the nature of the scattering, e.g, magnetic or nuclear.

### 3.1.2 Scattering kinematics

Because of its quantum nature, a neutron beam can be described with a complex plane wave function $\Psi(\mathbf{r}) = A\exp(i\mathbf{k}\cdot\mathbf{r})$, with $\mathbf{k}$ the neutron wavevector, $\mathbf{r}$ the spatial coordinate, and $A$ a normalization factor. After the scattering process and near a scattering centre—i.e, a nucleus—the wavefronts can be described as spherical waves $\Psi_{sc}(\mathbf{r}) = -Ab/r\exp(ikr)$, but far from the scattering centre, where neutrons are detected, they can be described as planar waves. Here we have introduced $b$, the *scattering length*, expressing the strength of the interaction between the neutron and the nucleus.

In a typical neutron scattering experiment, an incident neutron beam $\mathbf{k_i}$ is pointed toward the sample, and the scattered neutron $\mathbf{k_f}$ is detected at various angles from the incident direction (Figure 3.1).The scattering vector[5] is defined as:

$$\mathbf{Q} = \mathbf{k_i} - \mathbf{k_f} \tag{3.1}$$

and, if there is a change in energy between the incident and scattered neutrons, the

[5]Also referred to as the momentum transfer $\hbar\mathbf{Q}$.

energy transfer[6] is expressed as:

$$\hbar\omega = E_i - E_f = \frac{\hbar^2 k_i^2}{2m_n} - \frac{\hbar^2 k_f^2}{2m_n} \tag{3.2}$$

Combining eq. (3.1) and (3.2), one gets

$$Q^2 = k_i^2 + k_f^2 - 2kik_f\cos\theta = \frac{2m_n}{\hbar^2}(2E_i - \hbar\omega - 2\sqrt{E_i(E_i-\hbar\omega)}\cos\theta) \tag{3.3}$$

Equation (3.3) shows that the momentum ($Q$) and energy transfer ($\hbar\omega$) are not independent from each other. In practice, fixing $E_i$ restricts the accessible $(\mathbf{Q},\omega)$ space, and must be chosen carefully when designing the experiment.

### 3.1.3 Scattering cross section and structure factor

The measured quantity in a neutron scattering experiment is the differential scattering cross section, denoted $\frac{\mathrm{d}^2\sigma}{\mathrm{d}\Omega\mathrm{d}E_f}$. This quantity is proportional to the number of neutrons scattered per second in a solid angle $\Omega$ oriented in a given direction, with a final energy between $E_f$ and $E_f + \mathrm{d}E_f$:

$$\frac{\mathrm{d}^2\sigma}{\mathrm{d}\Omega\mathrm{d}E_f} = \frac{k_f}{k_i}S(\mathbf{Q},\omega) \tag{3.4}$$

$S(\mathbf{Q},\omega)$ is called the *dynamical structure factor*[7], and is usually the quantity of interest in a neutron experiment because it is ideally independent of the instrument geometry and the incident neutron wavelength.[8] Essentially, $S(\mathbf{Q},\omega)$ is a response function (in the sense that it is the response to the perturbation introduced in the scattering system by the neutron), which measures space- and time-correlations and represents the spontaneous fluctuations of atomic positions in the system. In the formalism established by Van Hove, it is written as:

$$S(\mathbf{Q},\omega) = \frac{1}{2\pi\hbar}\sum_{j,k}\overline{b_k b_j}\int_{-\infty}^{\infty}\langle\exp(-i\mathbf{Q}\cdot\mathbf{r_j}(0))\exp(i\mathbf{Q}\cdot\mathbf{r_k}(t))\rangle\exp(-i\omega t)\mathrm{d}t \tag{3.5}$$

In this expression, $\overline{b_j}$ refers to the scattering length of the atom $j$ (the bar represents an isotope and spin average), $\mathbf{r_j}(t)$ is the position in space of the atom $j$ at time $t$, and $\langle ...\rangle$ represents a thermal average.

[6] Sometimes denoted $\omega$.

[7] Sometimes referred to as *scattering function* or *scattering law*.

[8] However, instrumental effects inherent to the geometry, or due to the resolution and efficiency of the instrument, can be observed (see Section 4).

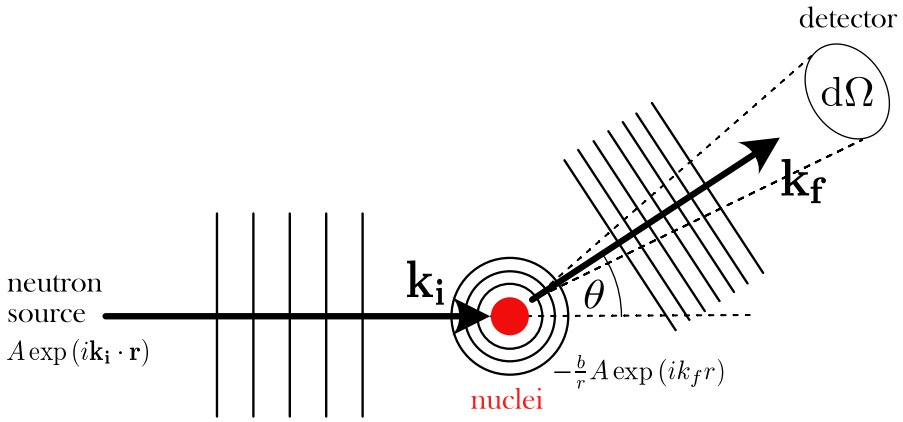


Figure 3.1: Schematic description of a neutron scattering process. The vertical lines perpendicular to $\mathbf{k_i}$ and $\mathbf{k_f}$, and the circles around the sample represent the wavefronts. dΩ is the solid angle covered by the detector.

### 3.1.4 Coherent and incoherent scattering

The scattering length describes the amplitude of the scattered neutron wave. It has the dimension of length and can be positive or negative, and even complex[9]. Typically, a sample contains several isotopes of a same element, in proportion to its natural abundance, which are randomly distributed. Because the scattering length varies with the isotope, each isotope scatters neutrons with a different amplitude, and, consequently, the interference pattern will be affected. This deviation to the ideal scattering is quantified in a so-called *isotope incoherent scattering*. Similarly, the nuclear spin is a source of incoherence. A neutron has spin orientation $\pm 1/2$, and when it interacts with a nuclei of spin $S$ the scattering length depends on the combined spin $S+1/2$ or $S-1/2$ and can take two values. This variation in $b$ gives rise to a so-called *spin incoherent scattering*. For example, hydrogen has three isotopes, namely $^1$H, $^2$H, $^3$H, with a major natural abundance of 99.985% of $^1$H. As a result, most of the hydrogen atoms in a sample are $^1$H and the isotope incoherent scattering is almost null. However, it has a nuclear spin of 1/2 and the spin orientations of the combined system neutron+hydrogen are 0 and 1 (corresponding to singlet and triplet states, respectively), with scattering lengths of $b_- = -47.52$ fm and $b_+ = 10.85$ fm, respectively. The large deviation between $b_-$ and $b_-$ causes a strong spin incoherent scattering signal.

[9]The imaginary part of a complex scattering length is related to the absorption of neutrons by the nuclei.

In eq. (3.5), assuming a random distribution of isotopes and spin orientations, $\overline{b_k b_j}$ can be simplified by:

$$\begin{aligned} \overline{b_k b_j} &= \overline{|b_j|^2} \text{ if } j = k, \\ &= \bar{b_k}\bar{b_j} \text{ if } j \neq k \end{aligned} \tag{3.6}$$

Using eq. (3.6) the sum in eq. (3.5) can separated into a sum of *coherent* and an *incoherent* contribution, according to:

$$S_{\text{coh}}(\mathbf{Q},\omega) = \frac{1}{2\pi\hbar}\sum_{j,k}\bar{b_k}\bar{b_j}\int_{-\infty}^{\infty}\langle\exp(-i\mathbf{Q}\cdot\mathbf{r_j}(0))\exp(i\mathbf{Q}\cdot\mathbf{r_k}(t))\rangle\exp(-i\omega t)\mathrm{d}t \tag{3.7}$$

and

$$S_{\text{inc}}(\mathbf{Q},\omega) = \frac{1}{2\pi\hbar}\sum_{j}(\overline{|b_j|^2} - |\overline{b_j}|^2)\int_{-\infty}^{\infty}\langle\exp(-i\mathbf{Q}\cdot\mathbf{r_j}(0))\exp(i\mathbf{Q}\cdot\mathbf{r_j}(t))\rangle\exp(-i\omega t)\mathrm{d}t \tag{3.8}$$

Eq. (3.8) embeds together the isotope and spin incoherence, but is it possible to separate them experimentally, as shown in Figure 3.2(b). Although purely mathematical, incoherent and coherent scattering have a physical interpretation, illustrated in Figure 3.2. From eq. (3.7) and (3.8), it is clear that coherent scattering depends on the average scattering lengths $\bar{b}$ , while the incoherent scattering depends on the deviations from $\bar{b}$. Eq. (3.7) and (3.8) also show that the incoherent scattering is due to the self-correlation in position at different times of each individual nucleus, while the coherent contribution is due to both the self-correlations of individual nuclei and the pair-correlations between the position of different nuclei. In summary, incoherent scattering carries information about individual atoms, irrespective of their arrangement, while coherent scattering yields information about collective behaviors such as the periodic structure of a crystal or their collective vibrations.

For any atomic species, the coherent and incoherent cross sections are defined as $\sigma_{inc} = 4\pi(\overline{|b|^2} - |\bar{b}|^2)$ and $\sigma_{coh} = 4\pi|\bar{b}|^2$. For hydrogen, $\bar{b} = \frac{3}{4}b_+ + \frac{1}{4}b_- = -3.74$ fm and $\overline{|b|^2} = \frac{3}{4}b_+^2 + \frac{1}{4}b_-^2 = 6.49$ barns, resulting in a large (spin) incoherent cross section of 80.3 barns, and a coherent cross section of 1.8 barns. The incoherent cross section of hydrogen is the largest among all atomic species. This feature is very useful for the study of dynamics in oxide- and nitride-hydride materials, because it ensures that most of the incoherent scattering can be interpreted in terms of hydride-ion dynamics. Moreover, due to their small coherent cross section, neutrons mostly "see" individual hydrogen species, rather than their spatial distribution in the sample. Thus, it allows for the observation of the self-diffusive motions of individual hydride-ions, *via* QENS, as well as their individual vibrational modes, *via* INS.

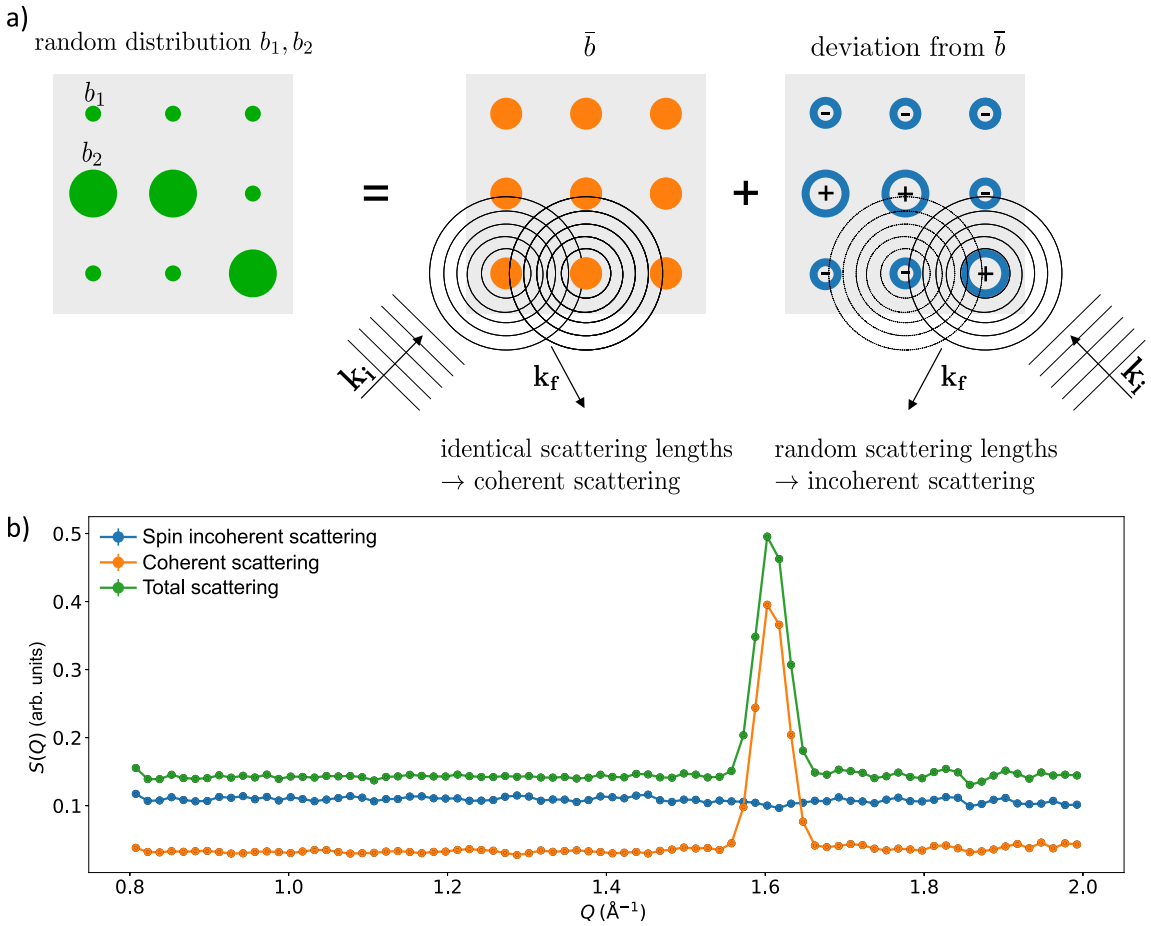


Figure 3.2: (a) Schematic illustration of the coherent and incoherent scattering contributions. In this example, the random distribution of two scattering lengths, $b_1, b_2$, can be either due to spin orientation or different isotopes. (b) Diffraction profile of a powder sample of $SrTiO_{2.9}H_{0.1}$ measured on the spectrometer LET at the ISIS pulsed neutron source, with a separation between coherent and spin incoherent scattering. The Bragg peak at 1.6 $Å^{-1}$ results from the periodic arrangement of the atoms in the crystal and is thus only visible in the coherent signal.

## 3.2 Inelastic neutron scattering

INS deals with the study of neutron-sample interactions involving an energy transfer. A neutron energy gain ($\hbar\omega < 0$) implies a sample energy loss, and a neutron energy loss ($\hbar\omega > 0$) implies a sample energy gain (Figure 3.3). INS is thus used to probe

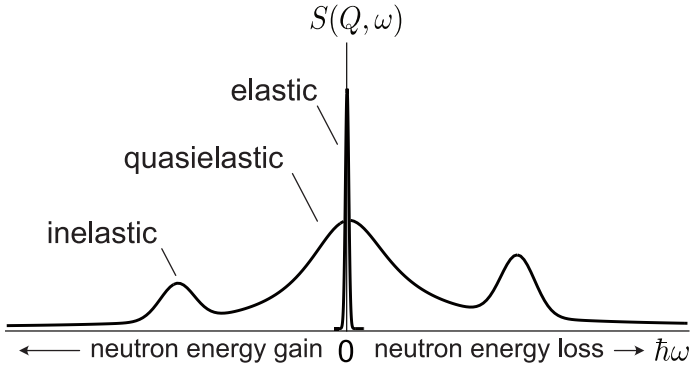


Figure 3.3: Illustration of the dynamical structure factor measured in a neutron scattering experiment. Adapted from ref. [58] with permission of The Licensor through PLSclear.

the vibrational excitation states of the sample.

The typical vibrational motions in condensed matter that INS probes are in the range of 1–500 meV. They correspond to oscillatory motions of small amplitude (compared to the interatomic distances) of atoms around their equilibrium position. In oxide- and nitride-hydride materials, we can observe collective vibrations, called *phonons*, and individual vibrations of the hydride-ions. This section briefly introduces some general aspects of vibrational dynamics of hydrogen as well as the associated dynamical structure factor measured with INS.

### 3.2.1 Isolated hydrogen atom trapped in a harmonic potential

In $BaTiO_{3-x}H_x$, the hydride-ions are randomly distributed over the oxygen sublattice and are present in relatively low concentrations. As a result, they do not interact with each other and can be considered as isolated hydrogen atoms trapped in harmonic potentials. The case of the isotropic harmonic potenital is described in Appendix C.

In the case of an anisotropic harmonic potential, such as an hydride-ion in $BaTiO_{3-x}H_x$, the system has 3 distinct fundamental vibrational modes, denoted $\nu_x$, $\nu_y$, $\nu_z$, with fundamental frequency $\omega_0^x$, $\omega_0^y$, $\omega_0^z$. The dynamical structure factor will show intensity when the energy transfer matches one of the vibrational mode, i.e for $\omega = p\omega_0^\nu$, with $p$ the transition order. $p = 1$ is called the *fundamental transition*, and $p > 1$ are called *overtones* or *higher-order transitions* (see Figure 3.4). The intensity

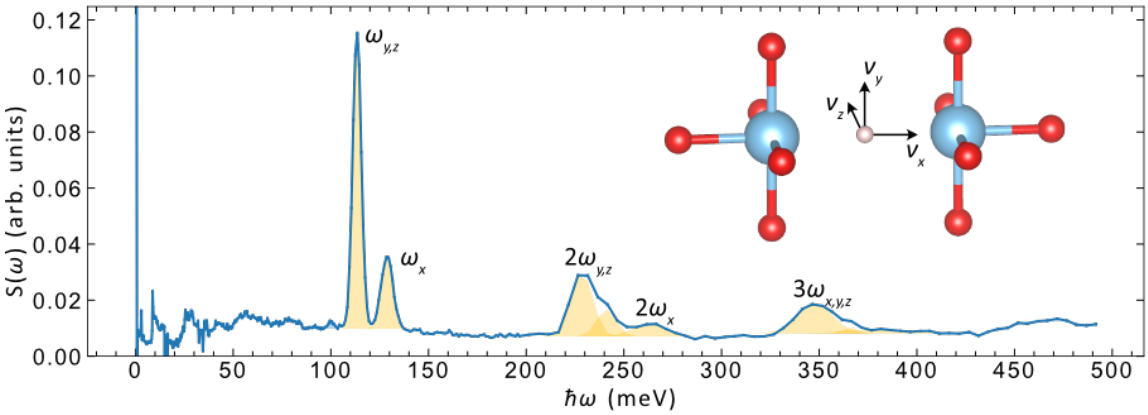


Figure 3.4: INS spectrum of a powder sample of $BaTiO_{2.9}H_{0.1}$ measured on LAGRANGE at the ILL, together with fits of the hydrogen peaks (shaded areas). Inset: illustration of the directions of the three vibrational modes in $BaTiO_{3-x}H_x$.

of each mode $\nu$ can be written as:

$$S(\mathbf{Q},\omega_\nu)_p \approx \frac{\sigma_{tot,H}}{4\pi}\exp(-[\mathbf{Q}\cdot\sum_{\nu=\nu_x,\nu_y,\nu_z}\mathbf{u}_\nu]^2)\frac{[\mathbf{Q}\cdot\mathbf{u}_\nu]^{2p}}{p!} \tag{3.9}$$

where $\mathbf{u}_\nu$ is the displacement vector of maximum amplitude of the mode $\nu$.

Note, the INS experiments in this thesis were performed on powder samples. The powder averaged form of eq. (3.9) is given by:

$$S(Q,\omega_\nu)_p \approx \frac{\sigma_{tot,H}}{4\pi}\exp(-Q^2\alpha_\nu^{(p)})\frac{Q^{2p}u_\nu^{2p}}{p!} \tag{3.10}$$

where $u_\nu^2$ is the mean square displacement of mode $\nu$, and $\alpha_\nu^{(p)}$ is a coefficient related to the transition order:

$$\alpha_\nu^{(1)} = \frac{1}{5}(u^2+2u_\nu^2) \quad \text{and} \quad \alpha_\nu^{(2)} = \frac{1}{7}(u^2+4u_\nu^2) \tag{3.11}$$

with $u^2 = u_{\nu_x}^2 + u_{\nu_y}^2 + u_{\nu_z}^2$, the total mean square displacement.

The term $\exp(-Q^2\alpha_\nu^{(p)})$ in eq. (3.10) is called *Debye-Waller factor*, and decreases with increasing $Q$ and increasing $u$. This is an effect of the thermal fluctuation of the hydride-ion, appearing as a diffuse object instead of a point object, which lowers the scattered intensity. This effect becomes more pronounced with increasing temperature because $u$ increases with temperature.

Figure 3.4 shows an INS spectrum, plotted as $S(\omega)$, of a powder sample of $BaTiO_{2.9}H_{0.1}$. The fundamental modes, first, and second overtones of hydride-ion vibrations can be easily identified around 120 meV, 230 meV, and 350 meV. The large peaks at 110 meV and 130 meV correspond to $\nu_z$ and $\nu_{x,y}$, respectively.

### 3.2.2 Collective vibrations of hydrogen atoms

This thesis presents INS data of the nitride-hydride $Ca_3CrN_3H$, in which hydride-ions are organized in linear chains along the crystallographic $c$-axis (see section 2.2.1). This case differs from the case of $BaTiO_{3-x}H_x$ because hydride-ions are now interacting with each others and are not individual harmonic oscillators. Their collective vibrational modes are called *phonon*. Because hydrogen has a large incoherent cross section, $S_{\text{inc}}(Q,\omega)$ is the main contribution to $S(Q,\omega)$. As a result, the observed INS spectrum of hydride-ion collective motions is seen as the sum of every individual hydride-ion motions, and can be treated as the spectrum of a set of individual oscillators[10], with eq. (3.10). A more complete description of phonons is given in Appendix D.

Figure 3.5 shows an INS spectrum, plotted as a 2D map of $S(Q,\omega)$, of a powder sample of $Ca_3CrN_3H$. The intensity in the range of 80–150 meV corresponds to fundamental modes of H, and the intensity in the range of 150–250 meV corresponds to the first overtones of the fundamental modes.

## 3.3 Quasielastic neutron scattering

In oxide- and nitride-hydride materials, QENS arises from hydride-ions performing random diffusional motions. In a spectrum, it appears as a broadening in energy of the elastic line (see Figure 3.3). Because of the large incoherent cross section of H, all quasielastic signals presented in this thesis can be interpreted in terms of incoherent scattering. This means that QENS probes here the self-diffusion motions of H. Such motions can be described by a self pair correlation function $G_s(\mathbf{r},t)$, representing the probability of finding H at the position $\mathbf{r}$ and the time $t$, given that it was at the position $\mathbf{r}=0$ at the time $t=0$. $S_{\text{inc}}(Q,\omega)$ is the time and space Fourier transform of $G_s(\mathbf{r},t)$. Thus, describing $G_s(\mathbf{r},t)$ for different types of H motions allows us to establish the expected $S_{\text{inc}}(Q,\omega)$.

The analysis of a QENS spectrum is based on the amplitude and the width ($\Delta E$) of the quasielastic signal. Their characteristics allow to disclose two types

[10]This is called the *incoherent approximation*.

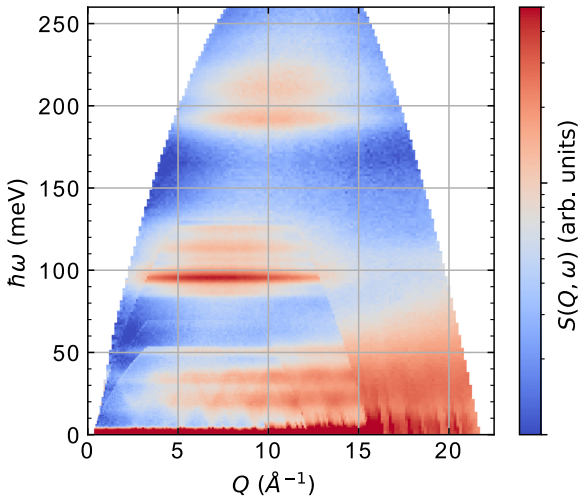


Figure 3.5: INS spectrum of a powder sample of $Ca_3CrN_3H$ measured on 4SEASONS at J-PARC. Four incidents energies were used (64.2 meV, 95.2 meV, 156 meV, and 299 meV).

of diffusion: long-range (translational) diffusion, and localised (spatially-restricted) diffusion. The amplitude provides infomartion about the geometry of the motion (long-range or localised), and when the diffusion involves jumping motions of the diffusing particle, $\Delta E$ is directly related to the average residence time.

### Long-range diffusion

Hydrogen diffusion in a solid is typically described by successive jumps between (stable) positions. When the time and space resolutions are much larger than the typical jump length and residence time of the diffusion, motions can be seen as continuous and be described with Fick's law. For the isotropic case, the self pair correlation function can be expressed by:

$$G_s(r,t) = \left(\frac{1}{4\pi D|t|}\right)^{3/2} \exp(-r^2/4D|t|), \tag{3.12}$$

with $D$ the diffusion constant of the process. After Fourier transformation, this expression becomes:

$$S_{\text{inc}}(Q,\omega) = \frac{1}{\pi}\frac{\hbar\Gamma(Q)}{(\hbar\omega)^2 + (\hbar\Gamma(Q))^2}, \tag{3.13}$$

with $\Gamma(Q) = DQ^2$.

As can be seen in eq. (3.13), $S_{\text{inc}}(Q,\omega)$ is a Lorentzian function of full-width at half-maximum in energy (FWHM) $2\hbar\Gamma(Q)$, and it becomes clear that the FWHM is correlated to the time scale of the dynamics, embedded in $D$. The $Q^2$ dependence of the FWHM is a typical signature of long-range continuous diffusion. For other long-range diffusion mechanisms, this trend is usually verified at small $Q$, but when the average jump distance increases, a deviation from the $Q^2$ trend occurs at higher $Q$. A more complex formalism, such as the Chudley-Elliott model, is then required to model the FWHM [60].

### Localised diffusion

Diffusion can also remain localised within a spatial boundary. In the case of oxide- and nitride-hydride materials, it typically corresponds to jump diffusion between a restricted number of sites. In the simplest case of two equivalent sites separated by a distance $l$ and with a mean residence time $\tau$, one can derive the incoherent dynamical structure factor:

$$S_{\text{inc}}(Q,\omega) = \frac{1}{2}[1 + j_0(Ql)]\delta(\hbar\omega) + \frac{1}{2}[1 - j_0(Ql)]\frac{1}{\pi}\frac{\hbar\Gamma}{(\hbar\omega)^2 + (\hbar\Gamma)^2}, \tag{3.14}$$

with $\Gamma = 2/\tau$ and $j_0(x) = \sin x/x$ the first spherical Bessel function. This expression is obtained after powder averaging, i.e. averaging over all scattering directions.[11] Importantly, eq. (3.14) includes a delta function which is absent in eq. (3.13) and reflects the fact that the probability to find the hydride-ion on each of the site after an infinite time is not null—as it would be for an unrestricted diffusion. Another notable difference with eq. (3.13) is the constant value of $\Gamma$ over $Q$. Finally, the pre-factors for the delta and the Lorentzian functions both depend on $Q$ and are correlated.

The pre-factor for the delta function is called *elastic incoherent structure factor* (EISF). It is the square modulus of the Fourier transform of the site distribution, so it is commonly used to determine the geometry of the localised dynamics. For the two-sites jump model, eq. (3.14) shows that it has an oscillating trend of period $2\pi/l$. Thus, the position of the first minimum of the EISF provides a good indication about the spatial extend of the localised dynamics.

[11] Powder averaging is employed with powder samples which contain many crystallite orientations.

### Practical aspects of QENS analysis

In practice, the measured dynamical structure factor is fitted to the function:

$$S_{\text{measured}}(Q,\omega) = \left[a_D(Q)\delta(\hbar\omega) + a_L(Q)\frac{1}{\pi}\frac{\hbar\Gamma(Q)}{(\hbar\omega)^2 + (\hbar\Gamma(Q))^2}\right] \circledast R(Q,\omega) + \text{bkg}(Q) \tag{3.15}$$

Here, the delta and Lorentzian functions are convoluted with the instrumental resolution, and the fitted parameters, $a_D(Q), a_L(Q), \Gamma(Q), \text{bkg}(Q)$ are analysed in terms of localised or long-range diffusion, as described above. $\text{bkg}(Q)$ represents a background which can be due to the instrument and the sample environment, or arise from the sample itself such as scattering by phonons.

Despite the large incoherent cross section of H, coherent scattering from other species in the sample persists in the elastic intensity at the Bragg peak positions. Consequently, data analysis is typically conducted away from the Bragg peaks. In the specific case of 1D diffusion, the fit is performed with:

$$S_{\text{measured}}(Q,\omega) = a_L(Q)S_{\text{1D,inc}}(Q,\omega) \circledast R(Q,\omega) + \text{bkg}(Q) \tag{3.16}$$

Figure 3.6 (a) shows an example fit of a quasielastic spectrum of a powder sample of $SrTiO_{2.9}H_{0.1}$, in which the diffusion was identified as localised. Figure 3.6 (b) shows the EISF fitted to the 2-sites jump diffusion model.

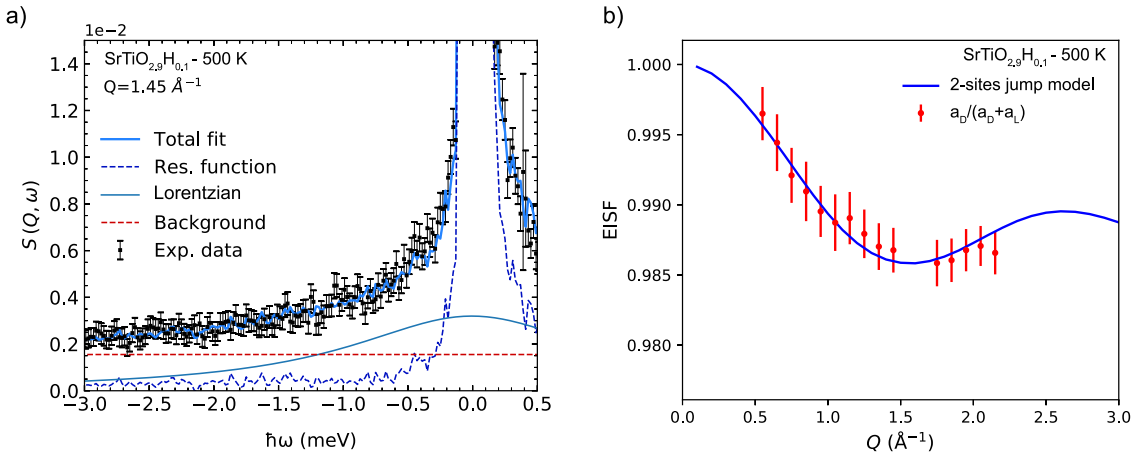


Figure 3.6: QENS data of a powder sample of $SrTiO_{2.9}H_{0.1}$ measured at 500 K on IN5 at the ILL. (a) Dynqmical structure factor, $S(Q,\omega)$, with fitting components. (b) EISF and fit to the 2-sites jump model.

# Chapter 4

# Neutron spectrometers

## 4.1 QENS and INS instruments

Neutron spectrometers are designed to explore the $(Q, \hbar\omega)$ space in INS, QENS, and diffraction experiments. As illustrated in Figure 4.1, different types of spectrometers allow to access different regions of this space. Since $Q$ and $\hbar\omega$ are associated to the space and time correlations of the dynamical processes under investigation, each type of spectrometer is more or less suited for probing the targeted dynamical process. Typically, optical phonons or molecular vibrations are found in the sub-picosecond time scales, corresponding to $\hbar\omega > 1$ meV, which is best probed with triple-axis or time-of-flight techniques. Diffusion is typically found in the picosecond to nanosecond time scales, corresponding to $0.01 < \hbar\omega < 1$ meV, which is best probed with backscattering or spin echo techniques. Deep inelastic technique, probing $\hbar\omega > 1$ eV to investigate atomic momentum distributions, was not used in this thesis and is not discussed further.

Time-of-flight (ToF) instruments use the flight time of neutrons to travel over a given distance to determine their velocity and, thus, their energy. The strength of these instruments is to cover quickly a large $(Q, \hbar\omega)$ space by measuring all $Q$ and $\hbar\omega$ simultaneously. This can be achieved thanks to the ToF technique coupled with large detector areas. Any neutron spectrometer is composed of a primary spectrometer placed before the sample, used to select or analyse the neutron incident energy ($E_i$), and a secondary spectrometer placed after the sample, used to select or analyse the neutron final energy ($E_f$). In the so-called *direct* geometry instruments, the primary spectrometer fixes $E_i$, and the secondary spectrometer measures $E_f$, whereas in the *indirect* (or *inverted*) geometry instruments, the primary spectrometer analyses $E_i$, and the secondary spectrometer fixes $E_f$. The indirect geometry has the advantage

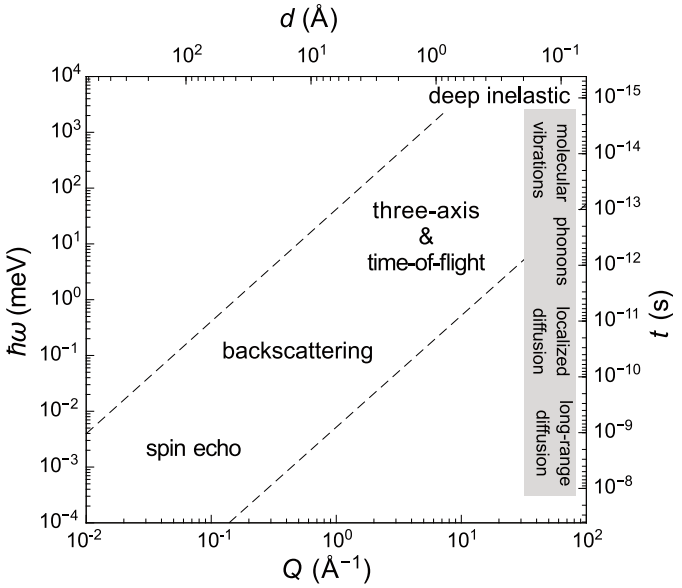


Figure 4.1: $(Q, \hbar\omega)$ space probed by different types of neutron spectrometers, together with the associated length ($d$) and time ($t$) correlations, and types of typical dynamical processes within different regions of the $(Q, \hbar\omega)$ space. The dashed lines represent the region accessible with neutron energy-loss scattering. Adapted from [58] with permission of The Licensor through PLSclear.

of accessing a large range of neutron energy loss[1] with a fixed $E_f$ and being only limited by the energy range of the primary spectrometer, whereas the fixed $E_i$ in the direct geometry limits the neutron energy loss to $\hbar\omega < E_i$. However, the indirect geometry can suffer from spurious features from the crystal analyser in the secondary spectrometer. The direct geometry is very flexible in choosing the more suitable $E_i$ and energy resolution for the probed dynamical process.

Triple-axis instruments use monochromating and analysing crystals as primary and secondary spectrometers. Their strength is to adjust the $Q$ and energy transfer resolutions to the dispersion properties of the measured excitations, i.e. phonons. Although they are not suited to cover a large area of the $(Q, \hbar\omega)$ space, a modified secondary spectrometer allows for a simultaneous measurement of many $Q$ values, as done with the indirect spectrometer LAGRANGE introduced in section 4.3.

Backscattering instruments use analysing and/or monochromating crystals in

[1]The neutron energy loss side of a spectrum is essential to probe vibrations of energy $> k_B T$ because, as an effect from the detailed-balance, the intensity in the energy gain side is reduced.

backscattering position, i.e. with a scattering angle near 180°, where the energy resolution of these crystals is best. They can access high energy resolutions but usually have a restricted energy transfer window. Thus, they are well suited for measuring the small $\hbar\omega$ involved in QENS measurements, but cannot access higher $\hbar\omega$ targeted in INS experiments.

In this thesis, a ToF spectrometer (4SEASONS), a variant of three-axis spectrometer (LAGRANGE), and a backscattering spectrometer (DNA) were used. The following sections give technical details of each of these instruments.

## 4.2 The ToF spectrometer 4SEASONS

4SEASONS is a direct geometry ToF spectrometer at the Japan Proton Accelerator Research Complex (J-PARC) facility [61]. The J-PARC neutron source produces neutron pulses at the frequency 25 Hz. 4SEASONS uses neutrons emerging from a coupled hydrogen moderator, delivering pulses with a relatively wide energy distribution of neutrons, shown in Figure 4.2.

4SEASONS [Figure 4.3 (a)] was used to perform an INS experiment on $Ca_3CrN_3H$ (Figure 3.5) and measure the hydride-ion vibrational modes. Chosen for its direct geometry coupled with a large $E_i$, it allowed to access the hydride-ion frequencies in the neutron energy-loss side. Moreover, its large detector area provided a large coverage of the $(Q, \hbar\omega)$ space, which allowed to separate host-lattice, nitrogen, and hydride-ion modes.

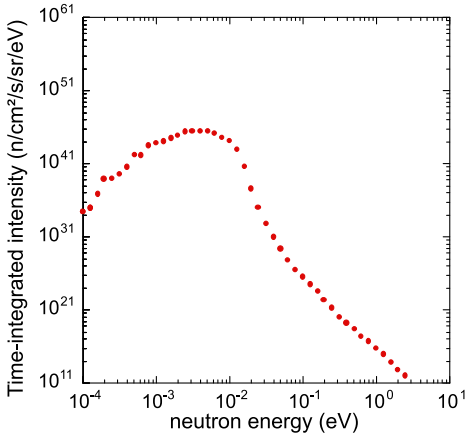


Figure 4.2: Spectral intensity of the neutron pulses after the coupled hydrogen moderator. Adapted from [62].

Figure 4.3(b) illustrates the ToF technique direct geometry: the $n^{\text{th}}$ pulse from the source contains neutrons within a certain range of energy (fast neutrons, in purple in Figure 4.3(b), and slow neutrons, in red). To select a specific incident energy, a physical window in the instrument is opened at the instant when the desired neutron velocity is reaching it, and remains closed otherwise. This window, called a *Fermi chopper*, is a rotating cylinder coated with a material absorbing neutrons and containing an array of slits. When the slits align with the beam, neutrons of specific energy can pass through and reach the sample. Neutrons are then scattered by the sample, where they change energy (and velocity), before reaching the detectors. The final energy is determined by measuring the neutron ToF between the source and the detectors and by calculating the final velocity (given the fixed distance separating the source, the Fermi chopper, the sample, and the detectors). 4SEASONS also includes a set of *disc choppers* and a *T0 chopper* (not represented in Figure 4.3 (b)) in order to suppress high energy incident neutrons contributing to the background noise and to pre-select a narrow band of incident energies before the final pulse shaping, monochromatization, and resolution setting by the Fermi chopper. Disc choppers are rotating discs perpendicular to the beam and opaque to neutrons with apertures in it.

Because 4SEASONS has a direct geometry, it cannot measure neutron energy-losses above $E_i$. However, its multiple incident energies capability [64] provides the

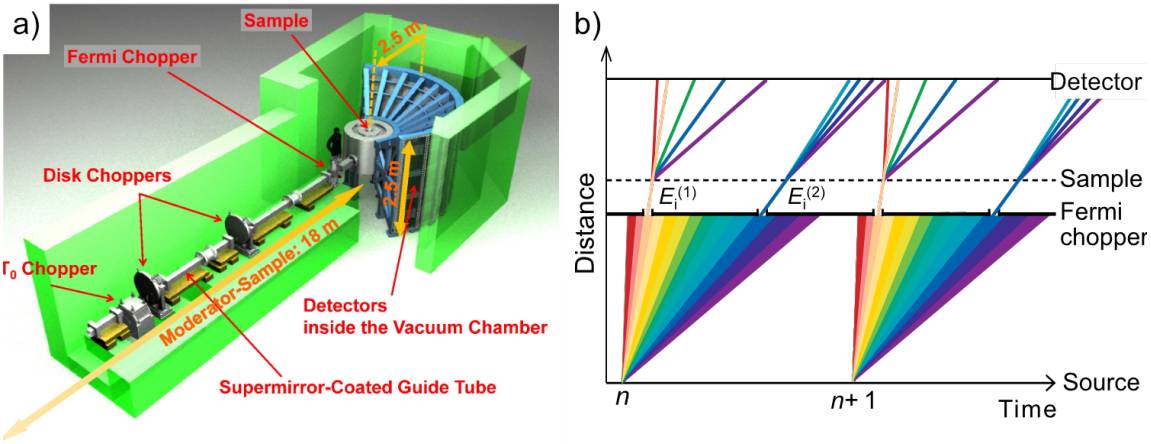


Figure 4.3: (a) Schematic view of the spectrometer 4SEASONS at J-PARC [63]. (b) Time distance diagram illustrating the ToF technique for a direct-geometry spectrometer at a pulsed source (adapted from [58] with permission of The Licensor through PLSclear).

energy range $5 < E_i < 300$ meV with a resolution of $\sim 5\%E_i$, making it well suited for INS experiments.

The scattering angle is measured on a large pixelated detector bank, collecting scattered neutrons between -35° and +91° horizontally and between -25° and +27° vertically, and consisting of an array of position sensitive detector tubes (PSD) filled with $^3$He gas.

Appendix F provides details on the typical data reduction routine for TOF spectrometers.

## 4.3 The spectrometer LAGRANGE

LAGRANGE (Large Area GRaphite ANalyser for Genuine Excitations) is an indirect-geometry spectrometer installed at the Institut Laue Langevin (ILL), France [65]. The ILL is a reactor source producing a continuous neutron beam, as opposed to the pulsed beam at J-PARC. LAGRANGE (Figure 4.4) was used to perform an INS experiment on $Ca_3CrN_3H$ and measure the hydride-ion vibrational modes. Chosen for its quick measurement, due to its modified secondary spectrometer and the high neutron flux at the ILL, it allowed to perform a temperature scan in a reasonable time (one day). Its design uses monochromating crystals to select incident neutron energies and to analyse final energies. The primary spectrometer consists of a

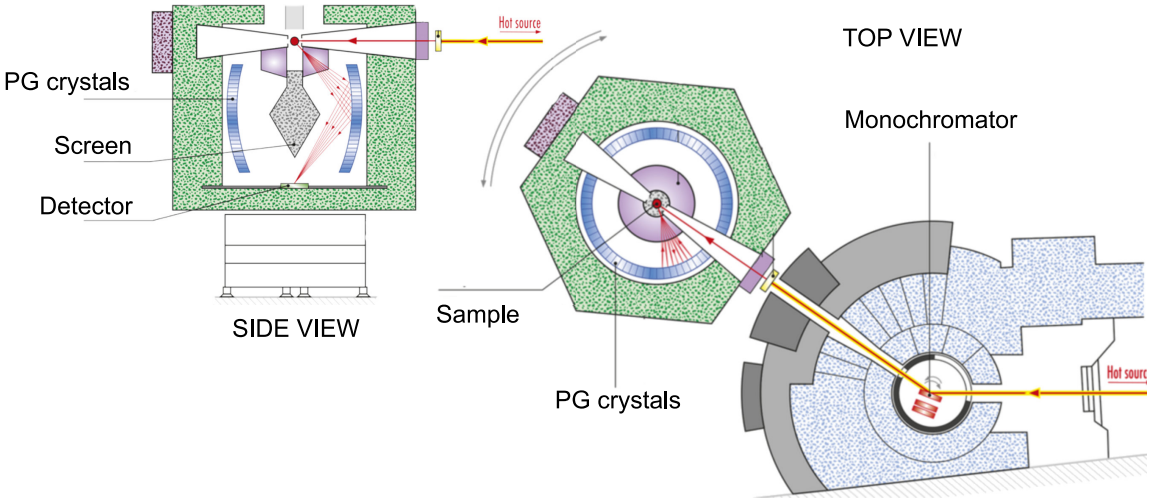


Figure 4.4: Schematic view of the spectrometer LAGRANGE at the ILL. Adapted from [66].

monochromator, which can be chosen between copper or silicon crystals, and which can be oriented relative to the incident beam to select an incident energy *via* the Bragg law. This $E_i$ scanning procedure can be seen as simulating the spread of neutron energies at a pulsed source [see Figure 4.3(b)]. The combination of Cu and Si crystals provides an accessible range of 26-500 meV with a resolution of 1–3%$E_i$.

The sample and secondary spectrometer are mobile in order to follow the orientation of the monochromator. The secondary spectrometer consists of a barrel-like reflecting surface of pyrolytic graphite (PG) surrounding the sample and oriented in order to reflect neutrons of final energy of 4.5 meV towards the detector. Such a design of the secondary spectrometer allows for collecting many neutrons, scattered in a cone shape from the sample (see the side view in Figure 4.4), thus providing an increased intensity compared to a classical three-axis spectrometer. However, as it collects neutrons at a fixed scattering angle, LAGRANGE probes a narrow curved region in the $(Q, \omega)$ space (visible in Appendix G). This feature makes it well suited for the study of non-dispersive vibrational modes, i.e. modes whose frequency does not depend on the wave vector. This is the case for molecular vibrations, or vibrational modes of largely incoherent scatterers, of which collective effects are invisible for neutrons, such as hydrogen vibrations.

Like 4SEASONS, the reduction of LAGRANGE data includes empty container subtraction as well as corrections for instrumental spurious effects. In practice, the data is normalized with a measurement of a water sample. An INS spectrum measured with LAGRANGE is visible in Figure 3.4.

## 4.4 The backscattering spectrometer DNA

DNA is a backscattering spectrometer at the J-PARC facility [67, 68] [Figure 4.5(a)]. It was used to perform QENS experiments on $Ca_3CrN_3H$ and $BaTiO_{3-x}H_x$ and observe the hydride-ion diffusion mechanism. Chosen for its combined high resolution mode and large energy window mode, it allowed to measure diffusional dynamics on a wide time scale, i.e from 100 picoseconds to 10 picoseconds.

As opposed to 4SEASONS, DNA has an indirect geometry, i.e. $E_f$ is fixed by crystal analysers and $E_i$ is determined *via* the ToF and distance between the source and the sample. On its low resolution mode, DNA utilizes the pulsed neutron beam produced by the source which contains a continuum of incident energies (see Figure 4.2). The emission of the $n^{th}$ pulse sets the starting time for the ToF analysis. As illustrated in Figure 4.5(c), neutrons of different energies reach the sample at different times. Then, they are scattered by the sample, and reach the crystal analysers, set to reflect neutrons with a specific $E_f$. Neutrons of energy $E_f$ are counted in the

detectors, at different instants $t$, defining the total ToF from the source. The energy transfer is calculated from the ToF *via*:

$$\hbar\omega = \frac{m_n}{2}\left(\frac{L_1^2}{(t-t_2)^2} - \frac{L_2^2}{t_2^2}\right) \tag{4.1}$$

and

$$S(\theta,\omega) = -\frac{L_1(t-t_2)^2}{t_2 m_n L_2}\frac{\mathrm{d}^2\sigma}{\mathrm{d}\Omega \mathrm{d}t}, \tag{4.2}$$

in which $t_2$ is fixed by $E_f$ and $L_2$ and $t_1 = t - t_2$. The energy resolution is $\sim 14$ μeV and the accesible energy range is -500–1500 μeV.

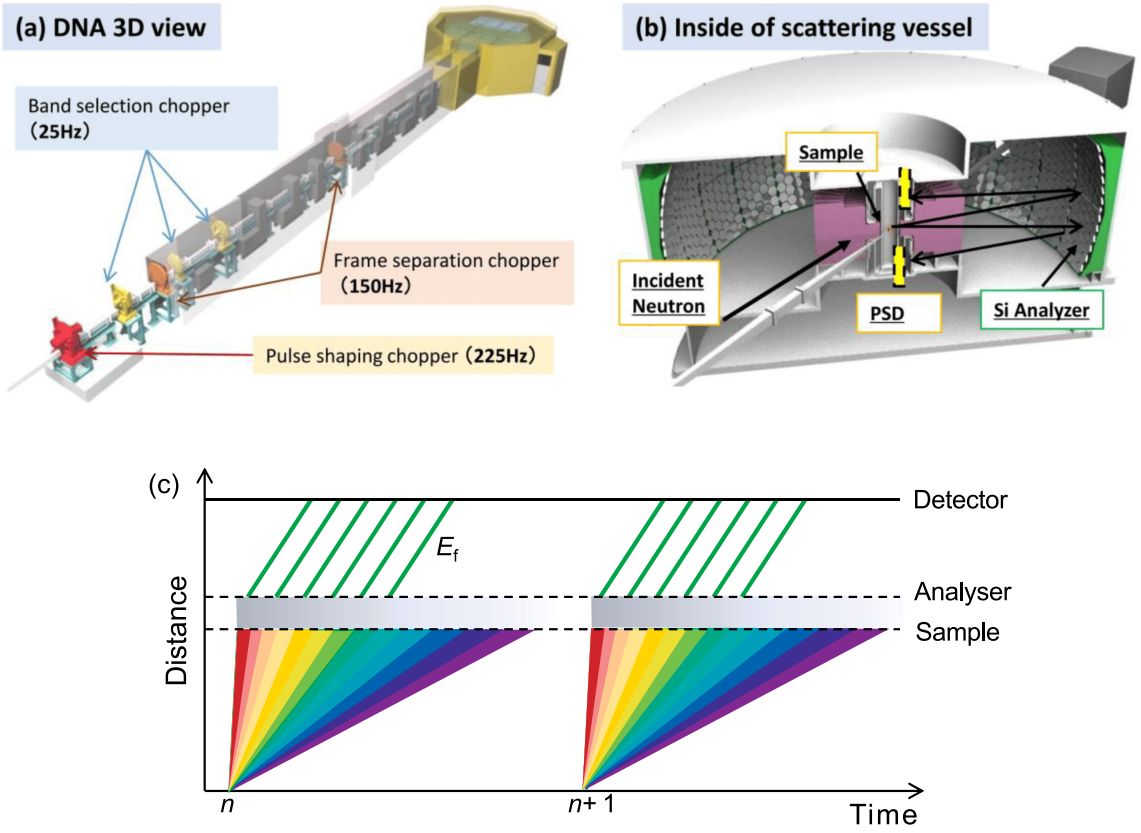


Figure 4.5: (a,b) Schematic view of the spectrometer DNA at J-PARC. Taken from [63]. (c) Time distance diagram illustrating the ToF technique for an indirect-geometry spectrometer at a pulsed source (adapted from [58] with permission of The Licensor through PLSclear).

DNA can also operate in high resolution mode by using a set of chopper systems. A pulse shaping chopper, consisting of two discs counter-rotating produces a narrow neutron pulse of $\sim 30$ µs (to be compared with the source pulse of $\sim 200$ µs) which reduces the uncertainty on the starting time of the ToF analysis and thus enhances the resolution. In this setup, the resolution reaches $\sim 3$ µeV, and the accessible energy range is -20–80 µeV. The *band selection* chopper reduces the background due to slow neutrons and the *frame separation chopper* is used to prevent the overlap of scattered neutrons coming from two consecutive pulses. By removing a few consecutive pulses, the frame separation chopper adds some dead time at the detectors between two pulses, thus preventing slow neutrons from the pulse $n$ and fast neutrons from the pulse $n+1$ to arrive at the detectors at the same time [see Figure 4.5 (c)].

The secondary spectrometer is a spherical surface of silicon crystal analysers using Bragg scattering to select neutrons of final energy $E_f = 2.08$ meV. After reflection on the analysers, neutrons are collected in a bank of tube detectors arranged around the sample. The high energy resolution of DNA is achieved by utilizing the crystal analysers in backscattering position, i.e. at a Bragg angle $\theta = 87.5° \approx 90°$, providing the lowest uncertainty in wavelength of the selected neutrons. This is expressed when differentiating the Bragg law:

$$(\Delta\lambda)^2 = (2\Delta d \sin\theta)^2 + (2d\Delta\theta\cos\theta)^2 \tag{4.3}$$

At $\theta = 90°$, $\cos\theta = 0$ and $\Delta\lambda$ is only due to the crystal imperfections $\Delta d$.

The analyser surface collects neutrons between -18° and +138° in the horizontal plane, and between -14° and +21° in the vertical plane, allowing for measuring $Q$ in the range of 0.08–1.86 Å$^{-1}$. The data reduction process is identical to 4SEASONS (Appendix F), except that the ToF to energy conversion is done at the beginning and all corrections are done in the $\hbar\omega$ space.

# Chapter 5

# Density functional theory

Density functional theory (DFT) is a powerful tool for neutron spectroscopists because neutron observables, such as vibrational frequencies, activation energies, or diffusion time scale and space scale, are relatively easy to compute with DFT, making theory and experiments comparable. This chapter provides a brief introduction about the fundamental aspects of DFT and how it has been applied in this thesis.[1]

## 5.1 General aspects of density functional theory

Electrons are the fundamental "glue" of condensed matter, bonding atoms together, and their electornic states is at the origin of electrical, magnetic, optical, and chemical properties of materials. Thus, finding a good model for a material and its properties means finding a good model for its electronic structure. DFT is an *ab initio*, or *first principles*, method to model electronic structures. *Ab initio* indicates that the formalism is based on fundamental equations of physics without additional assumptions, that is, based on the Schrödinger equation:

$$\hat{H}\Psi(\mathbf{r},\mathbf{R}) = E\Psi(\mathbf{r},\mathbf{R}) \tag{5.1}$$

Here, $\hat{H}$ is the Hamiltonian of the total electron and ion system, $\Psi$ is its wave function, $\mathbf{r}$ is the position of the electrons, and $\mathbf{R}$ is the position of the nuclei. As ions are heavier than electrons, they move on much slower time scales, and electrons accommodate instantaneously to such motions. As a result, the ionic and electronic Hamiltonians are often treated separately, and the ionic positions are fixed param-

[1]The provided formalism is mainly based on the textbook reference [69].

eters in the electronic Hamiltonian.[2] The Hamiltoninan for a many-electron system can be written as:

$$\hat{H}_{el} = -\frac{\hbar^2}{2m_e}\sum_{i=1}^{N}\nabla_i^2 - \sum_{i=1}^{N}\sum_{k=1}^{P}\frac{Z_k e^2}{|\mathbf{r}_i - \mathbf{R}_k|} + \frac{1}{2}\sum_{i=1}^{N}\sum_{\substack{j=1\\ j\neq i}}^{N}\frac{e^2}{|\mathbf{r}_i - \mathbf{r}_j|} \tag{5.2}$$

with $i$ indexing electrons, $k$ indexing ions, $e$ the elementary charge, $Z_k$ the charge of ion $k$, and $m_e$ the electron mass. The three terms of eq. (5.2) correspond respectively to the kinetic energy of electrons, the electron-nuclei interactions (further referred as external potential $V_{ext}(\mathbf{r})$), and the electron-electron interactions.

Eq. (5.1) is insoluble analytically for more than a few electrons. DFT provides a method to calculate numerically the ground state of large many-electron systems, which is based on the Hohenberg-Kohn theorems and the Kohn-Sham ansatz.

### The Hohenberg-Kohn theorems

The Hohenberg-Kohn theorems prove that the many-electron problem can be approached and solved in terms of electron density, and that all properties of the system can be expressed as unique functionals of the electron density [70]. Specifically, they state that a universal functional for the energy $E[n]$ in terms of the density $n(\mathbf{r})$ can be defined, and that the exact ground state energy of the system is the global minimum value of $E[n]$. The density $n(\mathbf{r})$ which minimizes $E[n]$ is the exact ground state density $n_0(\mathbf{r})$. The Hohenberg-Kohn theorems do not offer a direct expression for $E[n]$ or guidance on its practical utilisation. The Kohn-Sham approach, however, successfully addresses this limitation by providing a methodology for solving the many-electron problem based on these theorems.

### The Kohn-Sham ansatz

The Kohn-Sham approach reformulates the many-electron problem into a set of non-interacting electrons moving in an effective potential [71]. Crucially, a non-interacting system can be easily solved numerically, with a mathematical formulation more tractable than that of a many-electron system. The Kohn-Sham ansatz assumes that the real many-electron system and the fictitious non-interacting system have the same ground state density $n_0(\mathbf{r})$, and thus the same properties, pursuant to the first Hohenberg-Kohn theorem.

[2] This is the Born-Oppenheimer or *adiabatic* approximation, which provides accurate results for diffusional and vibrational motions in solids.

In the Kohn-Sham approach, the many-electron wave function is replaced by a single particle wave function and the correlation effects between electrons are all embedded in a so-called *exchange and correlation functional of the density*.

The Kohn-Sham approach provides an expression for the energy functional of the density $E[n]$:

$$E_{KS}[n] = T_s[n(\mathbf{r})] + E_{\text{Hartree}}[n(\mathbf{r})] + E_{xc}[n(\mathbf{r})] + \int \mathrm{d}\mathbf{r} V_{ext}(\mathbf{r}) n(\mathbf{r}) \tag{5.3}$$

where $T_s$ is the non-interacting kinetic energy of electrons, $E_{\text{Hartree}}$ the classical Coulomb interaction energy, $E_{xc}$ the exchange-correlation energy, and $V_{ext}$ the potential due to the presence of ions or any external field. Except $E_{xc}$, all these energy contributions are known exactly and have an analytical expression. The exchange-correlation term includes all complicated electron-electron interactions which are not described in the non-interacting kinetic and Coulomb terms. It is defined as the difference between the kinetic and internal interaction energy of the true many-electron system and the non-interacting system: $E_{xc}[n] = \langle \hat{T} \rangle + \langle \hat{V}_{\text{int}} \rangle - T_s[n] - E_{\text{Hartree}}[n]$.

In principle, if $E_{xc}$ was known exactly, the Kohn-Sham equations would give the exact ground state density and energy for the many-electron system. As a result, the heart challenge of DFT is to find a good approximation for $E_{xc}$. Since the formulation of the Hohenberg-Kohn-Sham approach, many exchange-correleation functionals were proposed and are still of common usage [72]. For example, in Paper II and IV, we used the functionals PBE [73] and PBEsol [74], known to model adequately vibrational motions in crystalline solids [75].

The Vienna Ab initio Simulation Package (VASP) [76–79] implements DFT for crystalline solids and was used in this thesis to study the electronic and vibrational properties of oxide- and nitride-hydride materials. The next section provides details on two methods used in Paper II to model vibrational motions in $Ca_3CrN_3H$.

## 5.2 Modeling vibrational motions

As mentioned in the previous section, DFT models electronic structures and treats ionic positions as fixed parameters. Consequently, an additional mathematical treatment is necessary to model ionic motions. In Paper II, we used both a *finite displacements* approach and a *molecular dynamics* approach.

**Finite displacements approach**

The finite displacements approach models phonons within the harmonic approximation, that is, assuming that atomic displacements are small compared to the interatomic distances and that the energy potential around each equilibrium position can be approximated as harmonic. Two simple cases were briefly described in Section 3.2.2.
In the general case, the energy potential $V$ of the ionic system, depending on the ionic positions $(\mathbf{R}_1, ..., \mathbf{R}_n)$, can be written as a Taylor expansion:

$$V(\{\mathbf{R}\}) = V(\{\mathbf{R}_{eq}\}) + \frac{1}{2} \sum_{i,\alpha,j,\beta} \frac{\partial^2 V(\{\mathbf{R}_{eq}\})}{\partial R_{i,\alpha} \partial R_{j,\beta}} \mathrm{d}R_{i,\alpha} \mathrm{d}R_{j,\beta} \tag{5.4}$$

with $\{\mathbf{R}_{eq}\}$ the equilibrium positions, and $\alpha$ and $\beta$ indexing the cartesian coordinates $\alpha, \beta = (x, y, z)$. The so-called *second-order force constants* (FCs) are defined as:

$$\Phi_{i,\alpha,j,\beta} = \frac{\partial^2 V(\{\mathbf{R}_{eq}\})}{\partial R_{i,\alpha} \partial R_{j,\beta}} = -\frac{\partial F_{j,\beta}}{\partial R_{i,\alpha}}, \tag{5.5}$$

with $F_{j,\beta}$ the force on atom $j$ in direction $\beta$ due to $R_{i,\alpha}$, the displacement of atom $i$ in direction $\alpha$.

FCs can be obtained *via* eq. (5.5), where DFT is used to calculate the interatomic forces $F_{j,\beta}$ from the ground state of the electronic system.[3] Numerically, atom $i$ is slightly displaced in direction $\alpha$ and "frozen" at the position $R_{i,\alpha} + \Delta R_{i,\alpha}$ (the displacement $\Delta R_{i,\alpha}$ is usually between 0.1 Å and 0.3 Å), the force on atom $j$ in direction $\beta$, $F_{j,\beta}(\Delta R_{i,\alpha})$ is evaluated by DFT, and the the FC is approximated as:

$$\Phi_{i,\alpha,j,\beta} \simeq -\frac{F_{j,\beta}(\Delta R_{i,\alpha}) - F_{j,\beta}}{\Delta R_{i,\alpha}}, \tag{5.6}$$

In the harmonic approximation, the FC matrix and ionic positions are the only parameters required to solve the equation of motion of ions and obtain the phonon dispersion relation. In this thesis, we used the software Phonopy to perform this last step. Details on its implementation can be found in refs [81, 82].

[3] Calculating the force acting on atom $i$ is possible according to the Hellmann–Feynman theorem [80], providing: $F_i = -\frac{\mathrm{d}E}{\mathrm{d}\mathbf{R}_i} = -\left\langle \psi \middle| \frac{\mathrm{d}\hat{H}}{\mathrm{d}\mathbf{R}_i} \middle| \psi \right\rangle$, with $\psi$ the ground state electronic wave function.

### Molecular dynamics approach

When the calculation cell is too large to compute the entire FC matrix, an *ab initio* molecular dynamics (AIMD) approach can be used. AIMD calculates atomic trajectories by integrating the classical equations of motion for the ion positions and velocities using forces derived from DFT calculations. The main steps of AIMD can be summarized as:

1. **Initialization**: positions and velocities of all atoms in the system are initialized for time $t = 0$.

2. **DFT calculation**: a DFT calculation is performed to determine the electronic ground state structure of the system and the forces acting on atoms.

3. **Equations of motion**: the equations of motion for the ion positions and velocities are established based on Newton's second law, $m_i\ddot{\mathbf{R}}_\mathbf{i} = \mathbf{F}_i$.

4. **Time Integration**: a numerical integration algorithms such as the Verlet algorithm [83] is employed to integrate the equations of motion and update the atomic positions and velocities at a later time step (a time step is usually a few fs).

5. **Thermostat**: As experiments are often performed at fixed temperature, one needs to model the canonical (or NVT) ensemble, where the temperature of the system is fixed. However, steps 1, 2, 3 model intrinsically a microcanonical (or NVE) ensemble, where the the total energy of the system is fixed. Consequently, a thermostat algorithm, such as the Nosé–Hoover thermostat [84], is employed to adjust the temperature of the system.

6. **Iterations**: steps 2–5 are repeated until the total simulation time is reached (typically a few tens of ps for modeling atomic vibrations).

The vibrational motions are then computed from the atomic trajectories *via* the velocity autocorrelation function (VACF). The VACF of atom $i$ is mathematically defined as:

$$C_{ii}(t) = \frac{1}{3}\langle v_i(t_0)v_i(t_0+t)\rangle_{t_0} \tag{5.7}$$

where $\langle\rangle_{t_0}$ denotes an average over initial times $t_0$. For oscillatory motions, such as atomic vibrations of a crystal lattice, the Fourier transform of the VAFC defines the vibrational density of states (DOS):

$$DOS(\omega) = \sum_i \mathrm{w}_i\tilde{C}_{ii}(\omega) \tag{5.8}$$

with $w_i$ a weighting factor for each atom. The DOS is a phonon spectral energy density, or phonon spectrum, that is, the number of phonon modes of a specific frequency $\omega$ in a small frequency interval $d\omega$.

In this thesis, a generalized vibrational density of state (GDOS) was computed from the neutron dynamical structure factor $S_{\mathrm{inc}}(Q,\omega)$ and compared to the theoretical DOS. The GDOS was defined within the incoherent approximation, i.e, by using eq. (5.8) with $w_i = \sigma_{i,inc}\exp(-2W_i)/4\pi m_i$. This was done in Paper II and used to interpret the INS data, where we used the software VASP to perform the AIMD calculations and the software MDANSE [85] to analyse the trajectories.

# Chapter 6

# Summary of results

## 6.1 Hydride-ion dynamics in $Ca_3CrN_3H$

Paper I and II take up the remaining open questions on $Ca_3CrN_3H$ as introduced in Chapter 2:

1. What is the local structure around hydride-ions in $Ca_3CrN_3H$, and does it include hydride-ion vacancies?

2. What is the hydride-ion diffusion mechanism in $Ca_3CrN_3H$, and how is it affected by temperature and vacancy concentration?

Question 1 is investigated with a combination of INS, finite displacements, and AIMD techniques, examining the hydride-ion vibrational modes which are usually correlated to the surrounding coordination environment (Paper II). Question 2 is investigated with QENS, by observing hydride-ion bulk mobility (Paper I).

### 6.1.1 INS results - Paper II

First, interpreting the INS data in conjunction with finite displacements and AIMD calculations validates the overall average crystal structure of the material, shown in Figure 2.6. In addition, two types of hydride-ion vibrational motions are revealed (Figure 6.1). Vibrations in the crystallographic *ab*-plane (labelled $\omega_{\perp,1}$ and $\omega_{\perp,2}$) have a non-dispersive character, whereas vibrations along the *c*-axis ($\omega_{\parallel}$) are found dispersive, i.e. vibrational frequencies spread out over the energy range of 80–130 meV as a function of the wave vector [Figure 6.1(b)]. Such a distribution of intensity is interpreted as a coupling between the hydride-ions, which cannot be described as

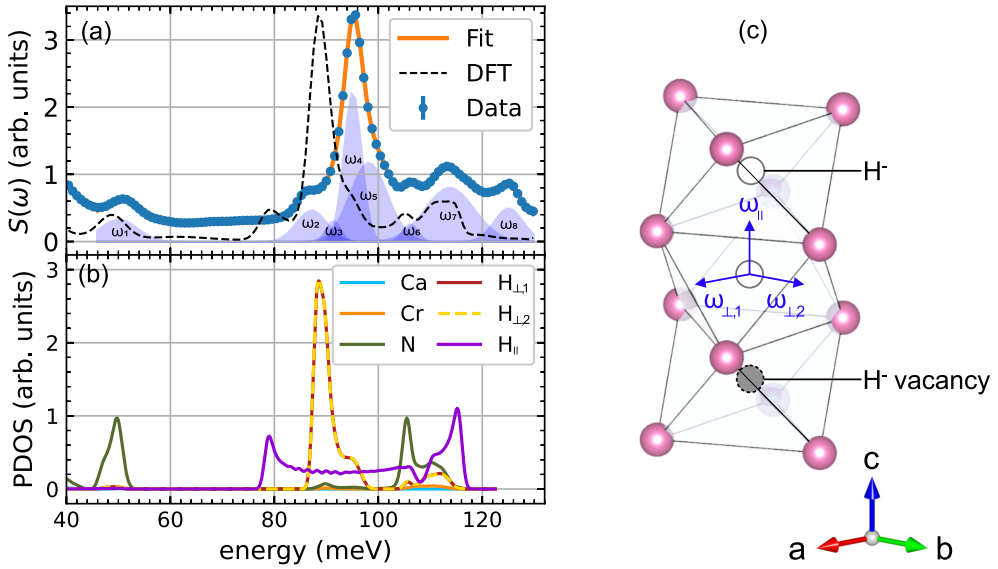


Figure 6.1: (a) INS spectra of $Ca_3CrN_3H$ measured on 4SEASONS, together with a fit of the peaks with Gaussian (shaded areas) and a DFT-simulated INS spectrum of $Ca_3CrN_3H$ (dashed line). (b) Projected vibrational density of states (PDOS) of $Ca_3CrN_3H$ calculated with DFT, and weighted by the total neutron scattering cross section and the mass of each element. (c) Illustration of the hydride-ion vibrational modes.

independent oscillators along the *c*-axis. This means that the interaction between neighbouring hydride-ions is strong enough to influence their vibrational frequencies, and consequently their jump rate. Importantly, DFT and AIMD show that the dispersive character disappears and that the hydride-ion vibrational frequency decreases when vacancies are introduced into the structure, due to longer H-H distances (see Paper II, Figure 3). In summary, introducing vacancies creates jumping sites but reduces the vibrational frequencies and thus the jumping rate. This observation gives the opportunity to tune the hydride-ion conductivity by controlling the vacancy concentration in $Ca_3CrN_3H$.

Moreover, the AIMD data is used to asses the proportion of hydride-ion vacancies in our sample of $Ca_3CrN_3H$ by comparing relative intensities in the INS and theoretical data. Since the intensity at highest energy ($\sim$ 125 meV) is found to be proportional to the hydride-ion concentration, it is compared with the intensity of $\omega_{\perp,1,2}$ ($\sim$ 90 meV) which is invariant with hydride-ion concentration. The intensity ratio indicates the stoichiometry $Ca_3CrN_3H_{0.8}$ (see SI of Paper II). Together with

the above conclusions, this composition suggests that the material might facilitate hydride-ion jump diffusion.

### 6.1.2 QENS results - Paper I

The QENS data reveals hydride-ion mobility over the entire probed temperature range of 100–450 K, which is interpreted as one-dimensional diffusive motion of the hydride-ions. Given the conclusions established from the INS and theoretical data, the QENS data is analysed in terms of one-dimensional (1D) diffusional motions along the $c$-axis, where hydride-ions are assumed to perform jumps between the vacant sites located in the center of the calcium octahedra [Figure 6.2(a)]. The diffusion constant ($D$) takes on values in the order of $10^{-6}$ $cm^2s^{-1}$ [Figure 6.2(b)]. This shall be compared with other hydride-ion conductors investigated by QENS, such as the oxide-hydrides $BaTiO_{3-x}H_x$ and $SrVO_2H$, which also show $D$ values in the range of $10^{-6}$ $cm^2s^{-1}$ [13, 14]. This comparison is interesting because $BaTiO_{3-x}H_x$ exhibits 3D diffusion, $SrVO_2H$ exhibits 2D diffusion, and $Ca_3CrN_3H$ exhibits 1D diffusion. The diffusion coefficient can be related to the microscopic jump mechanism with the relation $D = r^2/n\tau$, where $r^2$ is the squared jump distance, $\tau$ is the average residence time, and $n = 2, 4, 6$ for 1D, 2D, and 3D diffusion. This means that, for fixed $r^2$ and $d$, reducing the dimensionality has the effect of increasing $D$. $Ca_3CrN_3H$,

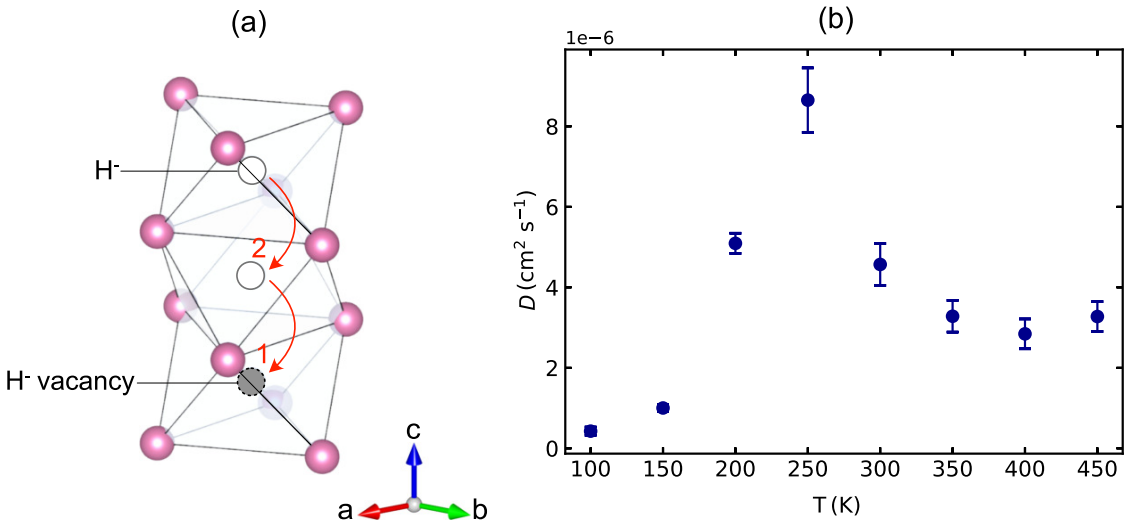


Figure 6.2: (a) Illustration of the hydride-ion jump mechanism in $Ca_3CrN_3H$. (b) Hydride-ion 1D diffusion constant in $Ca_3CrN_3H$ as measured with QENS.

$BaTiO_{3-x}H_x$, and $SrVO_2H$ are hard to compare because they have different values of $d$. However, the QENS data demonstrates that 1D diffusion of hydride-ions is possible to achieve in nitride-hydride materials, and suggests that reducing dimensionality in the hydride-ion conductors already known, such as $BaTiO_{3-x}H_x$, might be used to optimize the hydride-ion diffusivity.

Interestingly, under the interpretation of the data in terms of hydride-ion diffusion, the diffusion coefficient shows a maximum at 250 K which is still to be elucidated. It may be associated with a structural re-arrangement of the hydride-ion sub-lattice, affecting the diffusivity. It is also possible that it originates from magnetic scattering by the unpaired electrons of the $Cr^{4+}$ ions, where the fluctuations of the spin ordering in the Cr sub-lattice at 250 K would appear in the quasielastic signal. Such a quasielastic singal might be (incorrectly) interpreted as hydride-ion diffusion. This hypothesis is supported by the magnetic susceptibility of the closely related material $Ca_3CrN_3$, which shows a maximum at $\sim$ 240 K [86]. However, the magnetic susceptibility of $Ca_3CrN_3H$ is still unknown, and is required in order to test this hypothesis.

## 6.2 Hydride-ion dynamics in $BaTiO_{3-x}H_x$

Paper III and IV take up the remaining open questions on $BaTiO_{3-x}H_x$, as introduced in Chapter 2:

1. What is the origin of the discrepancies between experimental and theoretical results on hydride-ion diffusion in $BaTiO_{3-x}H_x$?

2. Do polarons exist in non-stoichiometric composition of $BaTiO_{3-x}H_x$, i.e including oxygen vacancies, and what is their impact on the electronic and ionic conductivity of the material?

Question 1 is investigated with a systematic QENS experiment on $BaTiO_{2.55}H_{0.12}$ and $BaTiO_{2.88}H_{0.12}$, conducted over a large temperature range (250–550 K) with the same instrument (DNA) to ensure consistency across the investigations (Paper III). Question 2 is investigated with DFT calculations, by evaluating the activation energy for the hydride-ion diffusion with a focus on the impact of the electronic structure surrounding the hydride-ion–oxygen vacancy pair (Paper IV).

### 6.2.1 QENS results - Paper III

In $BaTiO_{2.88}H_{0.12}$, free of oxygen vacancies, no dynamics are observed, which confirms that vacancies are required for hydride-ion diffusion. In $BaTiO_{2.55}H_{0.12}$, dynamics

are temperature dependant in the observed range of 300–550 K. Below 350 K, the diffusion mechanism is characterized by jumps of hydride-ions over an average distance of $\sim$ 3 Å, which corresponds to jumps between two nearest-neighbor (NN) sites, whereas between 350 and 550 K, the average jump distance reaches $\sim$ 3.6 Å, which indicates that jump between next-nearest-neighbor (2NN) sites are also involved (Figure 6.3). The diffusion coefficient for these dynamics is found in the range of $10^{-5}$ $cm^2s^{-1}$, and activation energies in the range of $60 - 100$ meV. This analysis supports the previous QENS results on $BaTiO_{3-x}H_x$, introduced in section 2.1 [13].

In addition, hydride-ion dynamics are also observed on a slower time scale, corresponding to a diffusion coefficient in the range of $10^{-6}$ $cm^2s^{-1}$. These dynamics are characterized by NN jumps exclusively, over the entire probed temperature range of 300–550 K. Since oxygen vacancies are more likely to be found in NN sites rather than in 2NN sites (because there are respectively 8 NN and 4 2NN sites surrounding the hydride ion). The exclusive occurrence of NN jumps is interpreted as a reduced oxygen vacancy concentration. Consequently, it is suspected that the fast and slow diffusion regimes correspond to diffusion of hydride-ions in vacancy-rich and vacancy-poor local environments. If this hypothesis is verified, inhomogeneity in the vacancy concentration in $BaTiO_{3-x}H_x$ may be used as a mean to optimize the conductivity of this material by controlling the formation of vacancy-rich domains. However, to

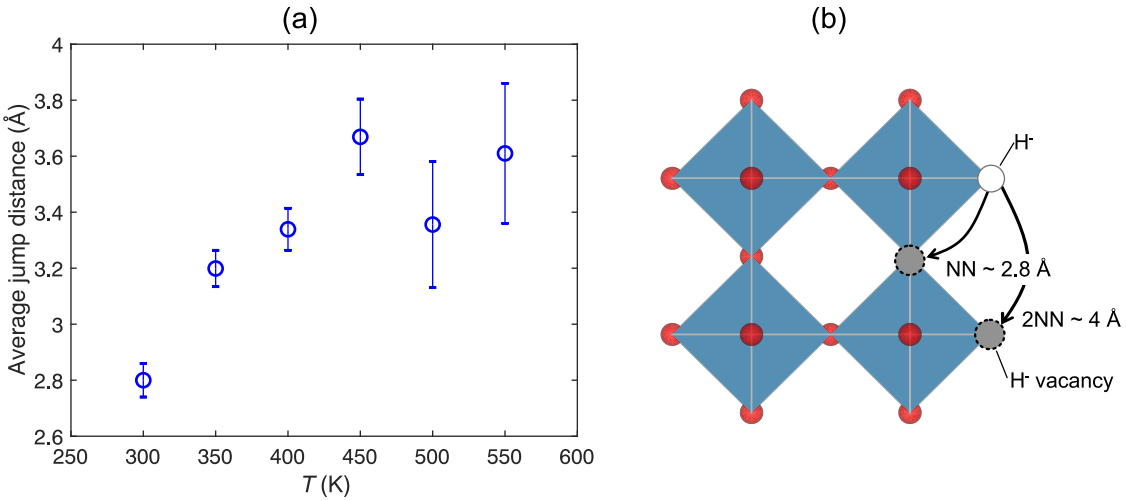


Figure 6.3: (a) Temperature dependence of the hydride-ion jump distance on $BaTiO_{2.55}H_{0.12}$. (b) Illustration of the two jump mechanisms involved. The Ba ion is omitted for clarity. Ti, O and H are represented by blue, red, and white spheres.

this day, no studies reported results about the vacancy distribution in $BaTiO_{3-x}H_x$. Interestingly, it was conjectured that surface modifications may lead to the presence of a $TiO_x(OH)_y$ shell around the $BaTiO_{3-x}H_x$ particles [49]. This feature brings an alternative explanation to the two-time-scale dynamics, which might correspond to diffusion within the $BaTiO_{3-x}H_x$ core and at the $TiO_x(OH)_y$ surface of the particles. If this hypothesis is verified, the $BaTiO_{3-x}H_x/TiO_x(OH)_y$ ratio may be controlled *via* the particle size, and finally, be used as a mean to optimize the conductivity of this material.

Elucidating on the origin of the two-time-scale dynamics constitute the main remaining open question of this work.

### 6.2.2 DFT results - Paper IV

In $BaTiO_3$, when an oxide is substituted with a hydride-ion to form $BaTiO_{3-x}H_x$, two titanium (Ti) electrons previously localised around the oxygen atom need to accommodate to a new local environment. One stays localised and forms $H^-$, while the other is released into the Ti sub-lattice. Similarly, when an oxygen vacancy is created, two electrons are released into the Ti sub-lattice. The electrons released, referred to as *doping electrons*, can either become delocalised across all Ti species or localise near a specific Ti atom. Their preferred state is presently unclear.

In Paper IV, DFT calculations using different exchange-correlation energy functionals, favoring or hindering electron localisation, show that the activation energy for the migration of hydride-ions between two vacancies is increased when the doping electrons are localised around the vacancies, whereas delocalised electrons do not affect the migration, as illustrated in Figure 6.4. This observation is explained by the fact that the electron charge interacts more with the hydride-ion when localized around the migration pathway rather than delocalised, leading to an increased Pauli repulsion and thus increased energy barrier.

The QENS results agree best with the activation energy calculated with delocalised doping electrons [see Figure 6.4(c)], and it is thus concluded that delocalised electrons are more likely to be found in the sample $BaTiO_{2.55}H_{0.12}$.

These results imply that electronic and ionic conductivities are related, which has direct implications for technological applications of $BaTiO_{3-x}H_x$. Typically, a fuel cell electrolyte requires a high ionic conductivity but should be electrically insulating. Thus, tuning the hydride-ion conductivity in $BaTiO_{3-x}H_x$ used as an electrolyte might result in an unwanted electronic conductivity and reduce the efficiency of the fuel cell.

Because the electronic localization takes place around the Ti ions, tuning the

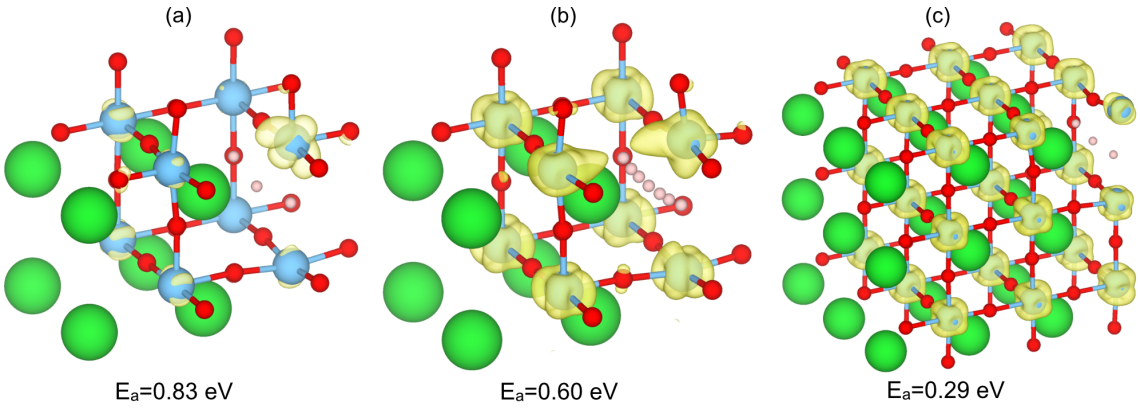


Figure 6.4: Simulation cells for the different electron localization scenarios, (a) localised, (b) partially delocalised, and (c) fully delocalised,. Overplotted are isosurfaces and calculated migration paths. The activation energy is indicated. Ba, Ti, O and H are represented by green, blue, red, and white spheres.

hydride-ion conductivity *via* the electronic properties of the material may be done by changing Ti for another transition metal. For example, the structurally related $BaZr_{0.5}In(II)_{0.5}O_{2.25}H_{0.5}$ includes zirconium (Zr) ions at the same crystallographic sites as the Ti ions in $BaTiO_{3-x}H_x$, and exhibits a mixed ionic and electronic conductivity [87]. A DFT and QENS study of this material would be well suited to explore further this question.

Lastly, these results contribute to the understanding of the large discrepancies between the DFT-calculated activation energy of 0.28 eV in [48] and 1 eV in [51], which employed different exchange-correlation energy functionals, modeling delocalised and localised doping electrons, respectively.

# Chapter 7

# Conclusions and outlook

In conclusion, the results of this thesis revealed that $Ca_3CrN_3H$ is a good hydride-ion conductor in the mixed-anion family, and that tuning the hydride-ion conductivity can be achieved by controlling the concentration of vacancies in the hydride-ion sublattice. It shows transport performances comparable to other oxide-hydride materials such as $SrVO_2H$ and $BaTiO_{3-x}H_x$. It is also the first nitride-hydride material studied with QENS.
Nonetheless, this work needs to be pursued and some experimental results clarified, i.e., the high value of the apparent diffusion coefficient at 250 K.
Data from a recent QENS experiment performed on the spectrometer IN5 at the ILL will help to understand this feature and to complement the present results.

Another open question which has to be tackled in future experiments is: What is the optimum vacancy concentration to achieve the best hydride-ion conductivity in $Ca_3CrN_3H$?

Furthermore, the study of $BaTiO_{3-x}H_x$ revealed that hydride-ion conductivity in this material can be controlled by tuning the oxygen vacancy concentration and increasing the temperature. Moreover, the hydride-ion conductivity is correlated to its electronic properties, which might be used as a mean to optimize it, e.g., *via* transition metal substitution. However, this hypothesis requires further experimental investigations. Finally, a main question remaining to be answered is: What is the origin of the two-time-scale dynamics in $BaTiO_{3-x}H_x$, and how can such a feature could be used to tune its hydride-ion conductivity? For this purpose, a new QENS experiment is planned at the spectrometer DNA. It will be performed on $BaTiO_{3-x}H_x$ samples with different grain sizes (20 nm, 50 nm, 100 nm and 500 nm), in order to identify the potential impact of grain-boundary on the QENS signal.

### Future work

To further expand my field of investigation in hydride-ion conducting materials, and to understand better how the hydride-ion diffusion mechanism is affected by the hosting lattice, I plan to perform QENS and INS experiments, as well as DFT calculations, on the layered hydride-halides materials $Ba_{2-\delta}H_{3-2\delta}X$ (X = Cl, Br, and I). As shown in Figure 7.1, they have demonstrated the best conductivity among all known hydride-ion conductors [88]. Interestingly, a comparable material showing a similar crystallographic structure, namely $BaH_2$, demonstrates a lower hydride-ion conductivity. This material was investigated with QENS [89], and with our experiment, we thus aim to understand the origins of the better performances of $Ba_{2-\delta}H_{3-2\delta}X$.

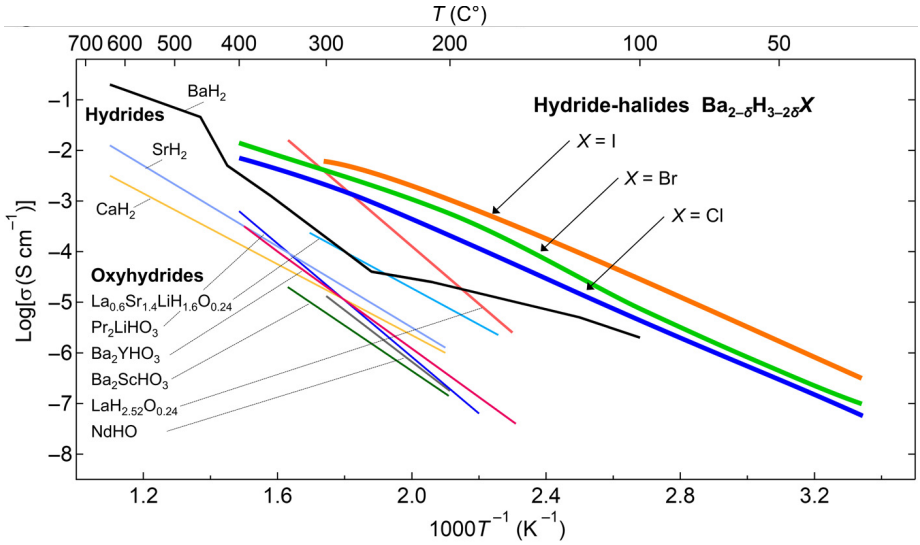


Figure 7.1: Total conductivity of the hydride-halides $Ba_{2-\delta}H_{3-2\delta}X$ compared with other hydride conductors. Reproduced from [88], in open access.

# Appendix A

# Hydride-ion diffusion in $BaTiO_{3-x}H_x$

| sample | method | temp (K) | $E_a$ (eV) | jumping site | ref |
|---|---|---|---|---|---|
| $BaTiO_{2.65}H_{0.35}$ | H/D Exchange | 600–1000 K | 3.84 | NN & ONN | [48] |
| $BaTiO_{2.61}H_{0.39}$ | H/D Exchange | 600–1000 K | 2.62 | NN & 2NN | [48] |
| $BaTiO_{2.56}H_{0.44}$ | H/D Exchange | 600–1000 K | 2.47 | NN & 2NN | [48] |
| $BaTiO_{2.40}H_{0.60}$ | H/D Exchange | 600–1000 K | 2.34 | NN & 2NN | [48] |
| - | DFT | - | 3.244 | 2NN | [48] |
| - | DFT | - | 0.995 | NN | [48] |
| $BaTiO_{2.82}H_{0.1}\square_{0.08}$ | QENS | 225–250 K | - | NN | [13] |
| $BaTiO_{2.65}H_{0.08}\square_{0.27}$ | QENS | 400–700 K | 0.85 | NN & 2NN | [13] |
| $BaTiO_{2.3}H_{0.04}\square_{0.66}$ | QENS | 400–700 K | 0.94 | NN & 2NN | [13] |
| - | DFT | - | 0.28 | NN | [51] |

Table A.1: Main results from literature regarding hydride-ion diffusion in $BaTiO_{3-x}H_x$. NN and 2NN refer to hydride-ion jumps between nearest-neighbor sites or next-nearest-neighbor sites, respectively. ONN refers to oxide-ion jump between nearest-neighbor sites.

# Appendix B

# Catalytic activity of $Ca_3CrN_3H$

When exposed to $H_2$ and $N_2$ at 400 ℃, $Ca_3CrN_3H$ exhibits catalytic activity for ammonia synthesis with performances comparable to other catalysts such as $Co_3Mo_3N$ ($Ca_3CrN_3H$ has a $NH_3$ synthesis rate of $\sim$ 865 $\mu$mol $g^{-1}h^{-1}$, to be compared with $\sim$ 796 $\mu$mol $g^{-1}h^{-1}$ for $Co_3Mo_3N$ in the same conditions) [21]. The reaction mechanism between $H_2$ and $N_2$ at the surface of $Ca_3CrN_3H$ was investigated with DFT, and revealed the crucial role of hydride-ions in the mechanism (Figure B.1). It was found that ammonia is synthesized *via* an associative route, meaning that the $N_2$

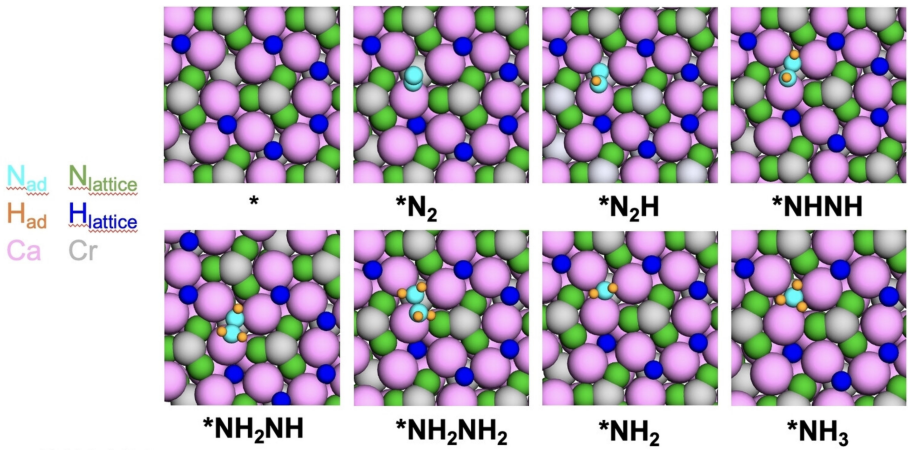


Figure B.1: Illustration of the reaction pathway for the ammonia synthesis catalytic activity at the surface of $Ca_3CrN_3H$. The pink, green, grey, dark blue, light blue and orange colors depict Ca, N, Cr, surface H, adsorbed N, and adsorbed H atoms, respectively. eproduced with permission from [21]. Copyright 2018 John Wiley and Sons.

molecule gets hydrogenated before breaking the N–N bond and releasing $NH_3$. The potential determining step of the reaction is the first, when $N_2$ gets adsorbed above a Ca atom and gets attacked by a $Ca_3CrN_3H$ hydrogen to form $N_2H$. Compared to the attack involving a gaseous hydrogen, this mechanism is found energetically favourable and thus preferred. It is not discussed how the newly empty H site gets replenished, but several mechanisms can be drawn out. For example, $H_2$ may get adsorbed in the vacancy, another option might be bulk hydride-ions diffusing to the surface and occupy the vacancy. In the following steps of the reaction, the product gets sequentially hydrogenated to $N_2H_2$, $N_2H_3$, $N_2H_4$; $H_2N{=}NH_2$ dissociates to two $NH_2$, and each product takes up a final H resulting in $NH_3$.

# Appendix C

# Isotropic harmonic oscillator

In a quantum picture, an isotropic harmonic oscillator has discrete excitation states and discrete energy levels, given by $E_n = (n + 1/2)\hbar\omega_0$, with $n = 0, 1, 2...$, $\omega_0 = \sqrt{K/m_H}$ the fundamental frequency, $K$ the force constant of the potential, and $m_H$ the mass of H. Because the potential is isotropic, only one cartesian direction can be considered—for example $x$—and the dynamical structure factor associated with this mode is given by:

$$\begin{aligned} S(\mathbf{Q},\omega) \approx & \frac{\sigma_{tot,H}}{4\pi}\exp(-Q^2\langle x^2\rangle) \\ & \times\left\{\delta(\hbar\omega)+\frac{\hbar Q^2}{2m_H\omega_0}[(n(\omega_0)+1)\delta(\hbar\omega-\hbar\omega_0)+n(\omega_0)\delta(\hbar\omega+\hbar\omega_0)]\right. \\ & \left.+\frac{\hbar Q^4}{2!2m_H\omega_0}[(n(\omega_0)+1)\delta(\hbar\omega-2\hbar\omega_0)+n(\omega_0)\delta(\hbar\omega+2\hbar\omega_0)]+...\right\} \quad \text{(C.1)} \end{aligned}$$

with $\langle x^2\rangle$ the mean square displacement of H along $x$, and $n(\omega_0) = 1/(\exp(\hbar\omega_0/k_BT)-1)$ the Plank distribution (Figure C.1). This expression is non-null for $\omega = 0$, $\omega = +\omega_0$, $\omega = -\omega_0$, $\omega = +2\omega_0$, $\omega = -2\omega_0$..., corresponding respectively to elastic scattering, a neutron energy loss of $\hbar\omega_0$ given to the oscillator, a neutron energy gain of $\hbar\omega_0$ given by the oscillator, and etc. Note that the neutron energy loss contributions are proportional to $n(\omega_0)$, emphasizing that the sample can only give energy if it is in an excited state, whereas the neutron energy loss contributions are proportional to $(n(\omega_0)+1)$, showing that neutrons can always excite a sample state. As a result, when $k_BT \ll \hbar\omega_0$, $S(\mathbf{Q},\omega)$ is very asymmetric around the elastic line,[1] with all the intensity found for $\omega > 0$ (see Figure C.1(b)). In the above description,

[1]This asymmetry is observed for any inelastic or quasielastic scattering process, independently of the type of motion. It stands as the *Principle of Detailed Balance*.

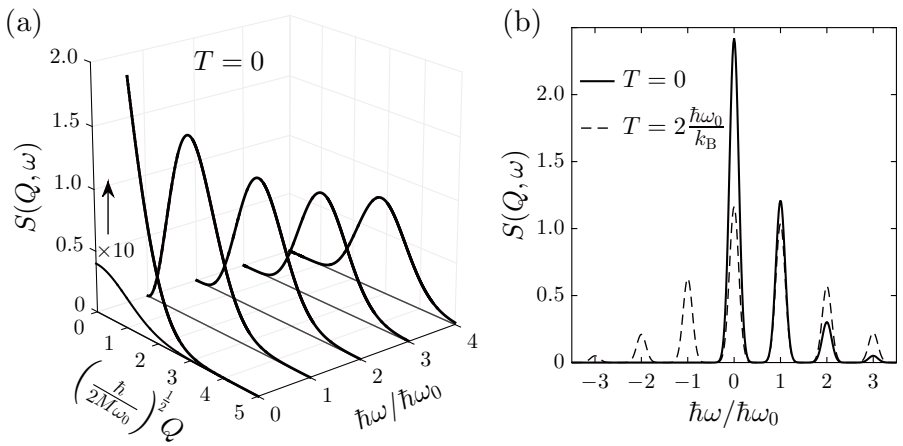


Figure C.1: $S(\mathbf{Q}, \omega)$ for the isotropic harmonic oscillator eq. (C.1), calculated for two temperatures. Reproduced from [58] with permission of The Licensor through PLSclear.

the scattering events exchanging a single quanta $\hbar\omega_0$ are called *fundamental transitions*, and the events involving multiple quanta are called *overtones* or *higher-order transitions*.

The term $\exp(-Q^2\langle x^2\rangle)$ in eq. (C.1) is called *Debye-Waller factor*, and decreases with increasing $Q$ and increasing $\langle x^2\rangle$. This is an effect of the thermal fluctuation of H, appearing as a diffuse object instead of as a point object. Neutrons are thus scattered from different locations around the equilibrium position and interfere destructively, which lower the scattered intensity. This effect becomes more pounced with increasing temperature because $\langle x^2\rangle$ increases with temperature. Consequently, the product $Q^2\exp(-Q^2\langle x^2\rangle)$ results in a Gaussian $Q$ dependence (see Figure C.1(a)).

# Appendix D

# Dispersion relation of a linear chain of hydrogen atoms

Consider an infinite chain of hydrogen masses connected by springs of force constant $f$ [Figure D.1 (a)]. Here, the springs model the inter-atomic forces. This model remains valid as long as the vibrational motions are small compared to the inter-atomic distances, resulting in a harmonic energy potential around the equilibrium position of each atom.[1] The equations of motion for such a system can be solved analytically and results in a set of decoupled solutions:

$$u_{l,k}(t) = u_{l,k} \exp(i(kla - \omega(k)t)) \tag{D.1}$$

with $l$ denoting the atom index, $a$ the inter-atomic distance at equilibrium, and $k$ a wave vector. For each $k$, eq. (D.1) models a *normal mode*, that is, a collective oscillation of all atoms at the same frequency $\omega(k)$, but phase-shifted by $kla$. As opposed to the individual oscillator case, the frequency is now function of $k$, expressed by the *dispersion relation*:

$$\omega(k) = 2 \sin\left(\frac{ka}{2}\right)\sqrt{\frac{f}{m_H}} \tag{D.2}$$

Eq. (D.2) is periodic and thus can be fully described in the range $-\frac{\pi}{a} < k < \frac{\pi}{a}$, defining the so-called *first Brillouin zone* [Figure D.1 (b)]. In the nitride-hydride $Ca_3CrN_3H$, the linear chains of hydrogen atoms are not isolated in space as the ideal case described above, but coupled to the host lattice. The physics of such a system

[1] This approximation is called the *harmonic approximation* and is used in most theoretical and computational approaches for calculating vibrational modes in crystals.

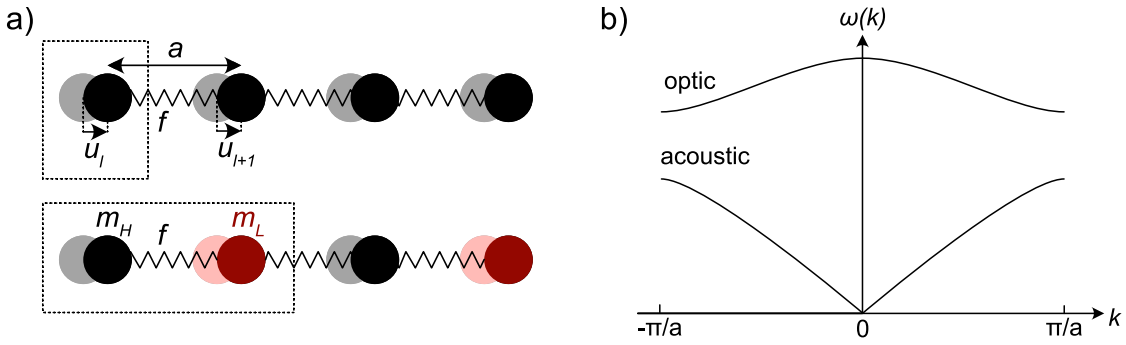


Figure D.1: (a) infinite chains of masses connected by springs. (upper) a monoatomic chain. (lower) a diatomic chain. The dashed lines represent a unit cell. (b) Dispersion relation for the diatomic chain as given by eq. (D.3).

can be captured in the simplified model of a diatomic linear chain [Figure D.1 (a)]. Now, the two atoms have different masses and are linked by springs of force constant $f$. Here, the host lattice is represented by the mass $m_L$, and the hydrogen atom by the mass $m_H$, with $m_L \gg m_H$. This system also results in a set of decoupled solutions, such as given in eq. (D.1), the only difference being that the normal modes are now indexed with a wave vector $k$ and a mode index $j$. The dispersion relation has now two *branches* ($j = 1$ and $j = 2$):

$$\omega_j^2(k) = f\left(\frac{1}{m_L} + \frac{1}{m_H}\right) + (-1)^j f\sqrt{\left(\frac{1}{m_L} + \frac{1}{m_H}\right)^2 - 4\frac{\sin^2(ka)}{m_L m_H}} \tag{D.3}$$

The lower branch, $j = 1$, is similar to the vibrations of the mono-atomic case and is called the *acoustic* branch, because it corresponds to acoustic waves propagating in the lattice. In the acoustic branch, $m_L$ and $m_H$ move in phase near $k = 0$. In the higher branch, $j = 2$, $m_L$ and $m_H$ move in phase-opposition near $k = 0$, and is called the *optic* branch, because it can usually be observed with optical spectroscopy techniques [Figure D.1 (b)].

In $Ca_3CrN_3H$ (Figure 3.5) we observe more than two bands because we find more than two masses per unit cell, and because the atoms can vibrate in three dimensions instead of along the chain axis only. For a 3D system with $p$ atoms per unit cell, the formalism is easily generalized and we find 3 acoustic branches and 3p-3 optic branches.

In a quantum-mechanical treatment, the total Hamiltonian of the system can be expressed as a sum of harmonic oscillator Hamiltonians, resulting in the same set of normal as expressed with eq. (D.1). The energy quanta $\hbar\omega(k)$, associated with

the Hamiltonian for the normal mode $(k, j)$, is called a *phonon* and is a bosonic quantum particle. Thus, the chain of atom can be described in terms of the phonon occupation of the normal modes, and the inelastic neutron scattering process by this system is treated as a neutron-phonon interaction.

# Appendix E

# Dynamical structure factor for 1D diffusion

For a diffusive motion restricted in one dimension (1D), the dynamical structure factor is given by [90]:

$$S_{\mathrm{1D,inc}}(Q,\omega) = \frac{1}{4\pi\sqrt{2}\omega y}\left[\ln\left(\frac{1+y^2-\sqrt{2}y}{1+y^2+\sqrt{2}y}\right)\right. \\ \left. + 2\arctan\left(1+\sqrt{2}y\right) - 2\arctan\left(1-\sqrt{2}y\right)\right] \quad \text{(E.1)}$$

and

$$y^2 = DQ^2/\omega, \quad \text{(E.2)}$$

, with $D$ a diffusion coefficient. It shows a more peaked profile (Figure E.1), which arises from the confinement in 1D. All scattering events with a $Q$ vector perpendicular to the diffusion axis will be elastic because the particle is immobile perpendicular to the diffusion axis. On the contrary, it has broad wings in the quasielastic region, accounting for particle notions along the diffusion axis.

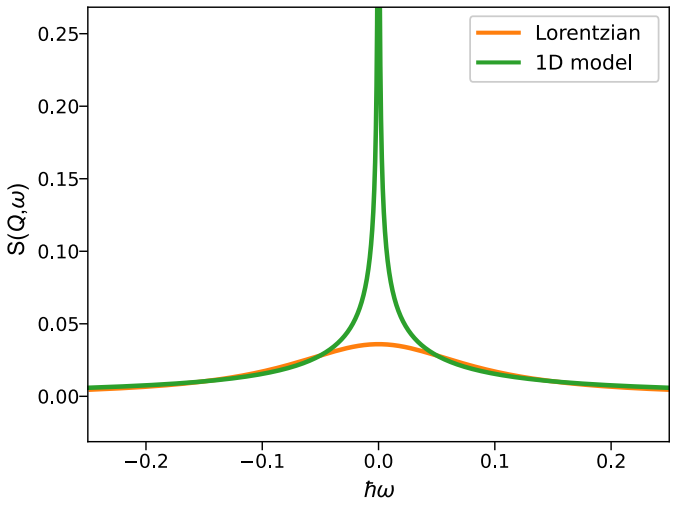


Figure E.1: Comparison of the $S(Q, \omega)$ lineshape between an isotropic diffusion [eq. (3.13)] and 1D diffusion [eq. (E.1)].

# Appendix F

# Data reduction for a TOF spectrometer

## Data reduction

In practice, data needs to be corrected from spurious effects due to the instrument and the sample itself. A typical data reduction routine includes:

1. **Background noise correction**. Background noise arise from scattering events occurring before and after the sample. It includes neutrons from outside the instrument or neutrons scattered by the sample environment and by the sample container (often made of aluminium). To subtract the background noise, a measurement of the empty container ($C$) is also performed, ideally at the same temperature as for the sample measurement ($X_S$). The corrected sample signal ($S$) is:

$$S(\theta, \text{ToF}) = X_S(\theta, \text{ToF}) - C(\theta, \text{ToF}) \tag{F.1}$$

   This expression is only an approximation because the sample inside the container always absorbs a fraction of the neutrons (which are thus not scattered), resulting in a background noise from the empty container slightly overestimated. This effect can be treated with *self-attenuation* corrections, not used in this thesis. Another type of spurious effect is *multiple scattering*, occurring when a same neutron is scatterd multiple times in the sample. Multiple scattering is limited by choosing the sample thickness small compared to the mean free path of neutron in the material. In practice, a sample transmission of $\sim 90\%$ is targeted.

2. **Detectors normalisation**. Different detectors have possibly different efficien-

cies, which is corrected by a measurement of a vanadium sample ($V$), a purely incoherent, elastic, and isotropic scatterer. The elastic peak of the vanadium is integrated over ToF and used to normalise the data.

$$S_{norm}(\theta, \text{ToF}) = \frac{S(\theta, \text{ToF})}{V(\theta)} \tag{F.2}$$

3. **Converting ToF to $\hbar\omega$**. The raw data consist of a number of counts as a function of $\theta$ and the ToF, i.e. the double differential cross section in time: $S_{norm}(\theta, \text{ToF}) = \frac{\mathrm{d}^2\sigma}{\mathrm{d}\Omega \mathrm{d}t}$, with $t$ the source-sample ToF. $S(\theta, \omega)$ is calculated *via*:

$$\hbar\omega = \frac{m_n}{2}\left(\frac{L_1^2}{t_1^2} - \frac{L_2^2}{(t-t_1)^2}\right) \tag{F.3}$$

and

$$S(\theta, \omega) = \frac{L_1(t-t_1)^4}{t_1 m_n L_2^3}\frac{\mathrm{d}^2\sigma}{\mathrm{d}\Omega \mathrm{d}t}, \tag{F.4}$$

with $L_1$ the source-sample distance, $L_2$ the sample-detectors distance, $t_1$ the source-sample ToF (fixed by $E_i$ and $L_1$), $t_2 = t - t_1$ the sample-detector ToF ($t$ measured as the elapsed time between a source pulse and a detector count), and $m_n$ the neutron mass. As can been seen in eq. (F.4), the relation between the double differential cross sections in energy and in ToF is not linear. As a result, although $S(\mathbf{Q}, \omega)$ is theoretically independent of the instrument type, some spurious effects can arise due to this non-linearity. Typically, a time-independent background, appearing as a constant in $\frac{\mathrm{d}^2\sigma}{\mathrm{d}\Omega \mathrm{d}t}$, will appear as a divergence following a $t^4$ trend in the energy spectrum.

4. **Detector efficiency correction**. The detector efficiency usually varies with the neutron energy. This is treated by an empirical factor $\epsilon(E_f)$.

5. **Grouping detectors**. Detectors are grouped and the momentum transfer $Q$ is determined *via* $\theta$, and the energy transfer $\hbar\omega$ ($\theta$, $Q$, and $\hbar\omega$ are related *via* eq. (3.3)). The dynamical structure factor $S(\mathbf{Q}, \omega)$ is obtained. We note that $\theta$ and $Q$ are not proportional, and the neutron collected in a detector at a given angle do not all contribute for the same $Q$ value due to their different $\hbar\omega$ contribution.

# Appendix G

# Kinematical range of LAGRANGE

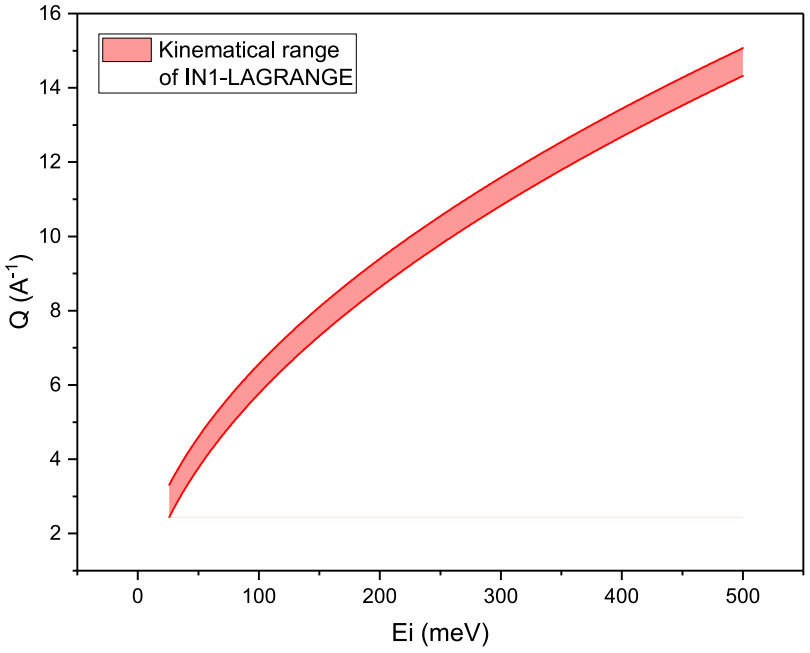


Figure G.1: Accessible $(Q, \hbar\omega)$ region covered by LAGRANGE. Taken from [91].

# Acknowledgements

I would like to thanks my supervisors Maths Karlsson and Michael Marek Koza for all their support, their availability, and for giving me the chance to do a PhD shared between the ILL and Chalmers. I would also like to thank my examiner Itai Panas for his great inputs and discussions on the theoretical aspects of my research. Thanks to Stéphane Rols, who has long been supporting me and encouraging me. Thanks to my colleagues and friends at Chalmers and at the ILL, Elena, Rasmus, Kannming, Peng, Aymen, Laura, Ronja; for helping me at work but also for their vital friendship. Also thanks to my collaborator Hiroshi Kageyama for providing samples, and to all scientists I have met and who helped me, especially Mónica Jiménez-Ruiz, Goran Nilsen, Masato Masuura, Andrew Seel, and Adrien Perrichon. Finally, I would like to thank my family and friends for all their presence and moral support.

# Bibliography


[1] Hydrogen, https://energy.ec.europa.eu/topics/energy-systems-integration/hydrogen_en.

[2] Global Hydrogen Review 2023, https://www.iea.org/reports/global-hydrogen-review-2023/executive-summary.

[3] A. Klerke, C. H. Christensen, J. K. Nørskov, and T. Vegge, J. Mater. Chem. **18**, 2304 (2008).

[4] IEA, Ammonia Technology Roadmap, https://www.iea.org/reports/ammonia-technology-roadmap/executive-summary (2021).

[5] S. Ghavam, M. Vahdati, I. A. G. Wilson, and P. Styring, Front. Energy Res. **9** (2021).

[6] H. Fang, D. Liu, Y. Luo, Y. Zhou, S. Liang, X. Wang, B. Lin, and L. Jiang, ACS Catal. **12**, 3938 (2022).

[7] W. Lubitz and W. Tumas, Chem. Rev. **107**, 3900 (2007).

[8] J. O. Abe, API. Popoola, E. Ajenifuja, and O. M. Popoola, Int. J. Hydrog. Energy **44**, 15072 (2019).

[9] A. M. Abdalla, S. Hossain, O. B. Nisfindy, A. T. Azad, M. Dawood, and A. K. Azad, Energy Convers. Manag. **165**, 602 (2018).

[10] M. Karlsson, Dalton Trans. **42**, 317 (2013).

[11] A. Perrichon, M. M. Koza, Z. Evenson, B. Frick, F. Demmel, P. Fouquet, and M. Karlsson, Chem. Mater. **35**, 6713 (2023).

[12] D. Noferini, B. Frick, M. M. Koza, and M. Karlsson, J. Mater. Chem. A **6**, 7538 (2018).

[13] C. Eklöf-Österberg, R. Nedumkandathil, U. Häussermann, A. Jaworski, A. J. Pell, M. Tyagi, N. H. Jalarvo, B. Frick, A. Faraone, and M. Karlsson, J. Phys. Chem. C **123**, 2019 (2019).

[14] R. Lavén, U. Häussermann, A. Perrichon, M. S. Andersson, M. S. Targama, F. Demmel, and M. Karlsson, Chem. Mater. **33**, 2967 (2021).

[15] E. Fabbri, D. Pergolesi, and E. Traversa, Chem. Soc. Rev. **39**, 4355 (2010).

[16] N. Sazali, W. N. Wan Salleh, A. S. Jamaludin, and M. N. Mhd Razali, Membranes **10**, 99 (2020).

[17] P. Boldrin and N. P. Brandon, Nat. Catal. **2**, 571 (2019).

[18] Z. Gao, L. V. Mogni, E. C. Miller, J. G. Railsback, and S. A. Barnett, Energy Environ. Sci. **9**, 1602 (2016).

[19] V. S. Marakatti and E. M. Gaigneaux, ChemCatChem **12**, 5838 (2020).

[20] Y. Kobayashi, Y. Tang, T. Kageyama, H. Yamashita, N. Masuda, S. Hosokawa, and H. Kageyama, J. Am. Chem. Soc. **139**, 18240 (2017).

[21] Y. Cao, E. Toshcheva, W. Almaksoud, R. Ahmad, T. Tsumori, R. Rai, Y. Tang, L. Cavallo, H. Kageyama, and Y. Kobayashi, ChemSusChem **16**, e202300234 (2023).

[22] Y. Tang, Y. Kobayashi, N. Masuda, Y. Uchida, H. Okamoto, T. Kageyama, S. Hosokawa, F. Loyer, K. Mitsuhara, K. Yamanaka, Y. Tamenori, C. Tassel, T. Yamamoto, T. Tanaka, and H. Kageyama, Adv. Energy Mater. **8**, 1801772 (2018).

[23] Y. Cao, M. A. Kirsanova, M. Ochi, W. Al Maksoud, T. Zhu, R. Rai, S. Gao, T. Tsumori, S. Kobayashi, S. Kawaguchi, *et al.*, Angew. Chem. Int. Ed. **61**, e202209187 (2022).

[24] H. Kageyama, K. Hayashi, K. Maeda, J. P. Attfield, Z. Hiroi, J. M. Rondinelli, and K. R. Poeppelmeier, Nat. Commun. **9**, 772 (2018).

[25] Inorganic Crystal Structure Database - ICSD, https://icsd.fiz-karlsruhe.de.

[26] G. Hitoki, T. Takata, J. N. Kondo, M. Hara, H. Kobayashi, and K. Domen, Chem. Commun. , 1698 (2002).

[27] K. Maeda, T. Takata, M. Hara, N. Saito, Y. Inoue, H. Kobayashi, and K. Domen, J. Am. Chem. Soc. **127**, 8286 (2005).

[28] M. Jansen and H. P. Letschert, Nature **404**, 980 (2000).

[29] R. Poettgen and D. Johrendt, Z. Für Naturforschung B **63**, 1135 (2008).

[30] H. Takahashi, K. Igawa, K. Arii, Y. Kamihara, M. Hirano, and H. Hosono, Nature **453**, 376 (2008).

[31] Z.-A. Ren, G.-C. Che, X.-L. Dong, J. Yang, W. Lu, W. Yi, X.-L. Shen, Z.-C. Li, L.-L. Sun, F. Zhou, and Z.-X. Zhao, EPL **83**, 17002 (2008).

[32] M. AI-Mamouri, P. P. Edwards, C. Greaves, and M. Slaski, Nature **369**, 382 (1994).

[33] N. Imanaka, K. Okamoto, and G.-y. Adachi, Angew. Chem. Int. Ed. **41**, 3890 (2002).

[34] Y. Kobayashi, O. Hernandez, C. Tassel, and H. Kageyama, Science and Technology of Advanced Materials **18**, 905 (2017).

[35] R. Dronskowski, S. Kikkawa, and A. Stein, *Handbook of Solid State Chemistry, 6 Volume Set* (John Wiley & Sons, 2017).

[36] C. A. Bridges, F. Fernandez-Alonso, J. P. Goff, and M. J. Rosseinsky, Adv. Mater. **18**, 3304 (2006).

[37] Y. Kobayashi, O. J. Hernandez, T. Sakaguchi, T. Yajima, T. Roisnel, Y. Tsujimoto, M. Morita, Y. Noda, Y. Mogami, A. Kitada, *et al.*, Nat. Mater. **11**, 507 (2012).

[38] N. Masuda, Y. Kobayashi, O. Hernandez, T. Bataille, S. Paofai, H. Suzuki, C. Ritter, N. Ichijo, Y. Noda, K. Takegoshi, *et al.*, J. Am. Chem. Soc. **137**, 15315 (2015).

[39] G. Kobayashi, Y. Hinuma, S. Matsuoka, A. Watanabe, M. Iqbal, M. Hirayama, M. Yonemura, T. Kamiyama, I. Tanaka, and R. Kanno, Science **351**, 1314 (2016).

[40] C. Tassel, Y. Goto, Y. Kuno, J. Hester, M. Green, Y. Kobayashi, and H. Kageyama, Angew. Chem. Int. Ed. **53**, 10377 (2014).

[41] T. Yamamoto, D. Zeng, T. Kawakami, V. Arcisauskaite, K. Yata, M. A. Patino, N. Izumo, J. E. McGrady, H. Kageyama, and M. A. Hayward, Nat Commun **8**, 1217 (2017).

[42] MA. Hayward, EJ. Cussen, JB. Claridge, M. Bieringer, MJ. Rosseinsky, CJ. Kiely, SJ. Blundell, IM. Marshall, and FL. Pratt, Science **295**, 1882 (2002).

[43] C. A. Bridges, G. R. Darling, M. A. Hayward, and M. J. Rosseinsky, J. Am. Chem. Soc. **127**, 5996 (2005).

[44] T. Sakaguchi, Y. Kobayashi, T. Yajima, M. Ohkura, C. Tassel, F. Takeiri, S. Mitsuoka, H. Ohkubo, T. Yamamoto, J. eun Kim, N. Tsuji, A. Fujihara, Y. Matsushita, J. Hester, M. Avdeev, K. Ohoyama, and H. Kageyama, Inorg. Chem. **51**, 11371 (2012).

[45] T. Yajima, A. Kitada, Y. Kobayashi, T. Sakaguchi, G. Bouilly, S. Kasahara, T. Terashima, M. Takano, and H. Kageyama, J. Am. Chem. Soc. **134**, 8782 (2012).

[46] X. Liu, T. S. Bjørheim, L. Vines, Ø. S. Fjellvåg, C. Granerød, Ø. Prytz, T. Yamamoto, H. Kageyama, T. Norby, and R. Haugsrud, J. Am. Chem. Soc. **141**, 4653 (2019).

[47] T. Yajima, F. Takeiri, K. Aidzu, H. Akamatsu, K. Fujita, W. Yoshimune, M. Ohkura, S. Lei, V. Gopalan, K. Tanaka, *et al.*, Nat. Chem. **7**, 1017 (2015).

[48] Y. Tang, Y. Kobayashi, K. Shitara, A. Konishi, A. Kuwabara, T. Nakashima, C. Tassel, T. Yamamoto, and H. Kageyama, Chem. Mater. **29**, 8187 (2017).

[49] H. Guo, A. Jaworski, Z. Ma, A. Slabon, Z. Bacsik, R. Nedumkandathil, and U. Häussermann, RSC Adv. **10**, 35356 (2020).

[50] R. Nedumkandathil, A. Jaworski, J. Grins, D. Bernin, M. Karlsson, C. Eklöf-Österberg, A. Neagu, C.-W. Tai, A. J. Pell, and U. Häussermann, ACS Omega **3**, 11426 (2018).

[51] X. Liu, T. S. Bjørheim, and R. Haugsrud, J. Mater. Chem. A **5**, 1050 (2017).

[52] K. Ueda, H. Yanagi, H. Hosono, and H. Kawazoe, J. Phys. Condens. Matter **11**, 3535 (1999).

[53] P. Pasierb, S. Komornicki, and M. Radecka, Thin Solid Films **324**, 134 (1998).

[54] J. Zhang, G. Gou, and B. Pan, J. Phys. Chem. C **118**, 17254 (2014).

[55] Y. Iwazaki, T. Suzuki, and S. Tsuneyuki, J. Appl. Phys. **108**, 083705 (2010).

[56] G. Bouilly, T. Yajima, T. Terashima, W. Yoshimune, K. Nakano, C. Tassel, Y. Kususe, K. Fujita, K. Tanaka, T. Yamamoto, Y. Kobayashi, and H. Kageyama, Chem. Mater. **27**, 6354 (2015).

[57] E. J. Granhed, A. Lindman, C. Eklöf-Österberg, M. Karlsson, S. F. Parker, and G. Wahnström, J. Mater. Chem. A **7**, 16211 (2019).

[58] A. T. Boothroyd, *Principles of Neutron Scattering from Condensed Matter* (Oxford University Press, 2020).

[59] P. C. H. Mitchell, S. F. Parker, A. J. Ramirez-Cuesta, and J. Tomkinson, *Vibrational Spectroscopy with Neutrons: With Applications in Chemistry, Biology, Materials Science and Catalysis*, Series on Neutron Techniques and Applications, Vol. 3 (WORLD SCIENTIFIC, 2005).

[60] C. T. Chudley and R. J. Elliott, Proc. Phys. Soc. **77**, 353 (1961).

[61] R. Kajimoto, M. Nakamura, Y. Inamura, F. Mizuno, K. Nakajima, S. Ohira-Kawamura, T. Yokoo, T. Nakatani, R. Maruyama, K. Soyama, K. Shibata, K. Suzuya, S. Sato, K. Aizawa, M. Arai, S. Wakimoto, M. Ishikado, S.-i. Shamoto, M. Fujita, H. Hiraka, K. Ohoyama, K. Yamada, and C.-H. Lee, J. Phys. Soc. Jpn. **80**, SB025 (2011).

[62] Y. Kiyanagi, J. Korean Phys. Soc. **59**, 779 (2011).

[63] K. Nakajima, Y. Kawakita, S. Itoh, J. Abe, K. Aizawa, H. Aoki, H. Endo, M. Fujita, K. Funakoshi, W. Gong, M. Harada, S. Harjo, T. Hattori, M. Hino, T. Honda, A. Hoshikawa, K. Ikeda, T. Ino, T. Ishigaki, Y. Ishikawa, H. Iwase, T. Kai, R. Kajimoto, T. Kamiyama, N. Kaneko, D. Kawana, S. Ohira-Kawamura, T. Kawasaki, A. Kimura, R. Kiyanagi, K. Kojima, K. Kusaka, S. Lee, S. Machida, T. Masuda, K. Mishima, K. Mitamura, M. Nakamura, S. Nakamura, A. Nakao, T. Oda, T. Ohhara, K. Ohishi, H. Ohshita, K. Oikawa, T. Otomo, A. Sano-Furukawa, K. Shibata, T. Shinohara, K. Soyama, J.-i. Suzuki, K. Suzuya, A. Takahara, S.-i. Takata, M. Takeda, Y. Toh, S. Torii, N. Torikai, N. L. Yamada, T. Yamada, D. Yamazaki, T. Yokoo, M. Yonemura, and H. Yoshizawa, Quantum Beam Sci. **1**, 9 (2017).

[64] M. Nakamura, R. Kajimoto, Y. Inamura, F. Mizuno, M. Fujita, T. Yokoo, and M. Arai, J. Phys. Soc. Jpn. **78**, 093002 (2009).

[65] A. Ivanov, M. Jimenéz-Ruiz, and J. Kulda, in *J. Phys. Conf. Ser.*, Vol. 554 (IOP Publishing, 2014) p. 012001.

[66] IN1-LAGRANGE - ILL Neutrons for Society, https://www.ill.eu/users/instruments/instruments-list/in1-lagrange/description/instrument-layout.

[67] Repetition Rate Multiplication: RRM, an Advanced Measuring Method Planed for the Backscattering Instrument, DNA at the MLF, J-PARC | Journal of the Physical Society of Japan, https://journals.jps.jp/doi/10.1143/JPSJS.80SB.SB007.

[68] The Performance of TOF near Backscattering Spectrometer DNA in MLF, J-PARC.

[69] R. M. Martin, *Electronic Structure: Basic Theory and Practical Methods* (Cambridge University Press, Cambridge, 2004).

[70] P. Hohenberg and W. Kohn, Phys. Rev. **136**, B864 (1964).

[71] W. Kohn and L. J. Sham, Phys. Rev. **140**, A1133 (1965).

[72] A. D. Becke, The Journal of Chemical Physics **140**, 18A301 (2014).

[73] J. P. Perdew, K. Burke, and M. Ernzerhof, Phys. Rev. Lett. **77**, 3865 (1996).

[74] J. P. Perdew, A. Ruzsinszky, G. I. Csonka, O. A. Vydrov, G. E. Scuseria, L. A. Constantin, X. Zhou, and K. Burke, Phys. Rev. Lett. **102**, 039902 (2009).

[75] R. Wahl, D. Vogtenhuber, and G. Kresse, Phys. Rev. B **78**, 104116 (2008).

[76] G. Kresse and D. Joubert, Phys. Rev. B **59**, 1758 (1999).

[77] G. Kresse and J. Hafner, Phys. Rev. B **47**, 558 (1993).

[78] G. Kresse and J. Furthmüller, Phys. Rev. B **54**, 11169 (1996).

[79] G. Kresse and J. Furthmüller, Comput. Mater. Sci. **6**, 15 (1996).

[80] R. P. Feynman, Phys. Rev. **56**, 340 (1939).

[81] A. Togo, J. Phys. Soc. Jpn. **92**, 012001 (2023).

[82] A. Togo, L. Chaput, T. Tadano, and I. Tanaka, J. Phys.: Condens. Matter **35**, 353001 (2023).

[83] L. Verlet, Phys. Rev. **159**, 98 (1967).

[84] D. J. Evans and B. L. Holian, The Journal of Chemical Physics **83**, 4069 (1985).

[85] G. Goret, B. Aoun, and E. Pellegrini, J Chem Inf Model **57**, 1 (2017).

[86] D. A. Vennos, M. E. Badding, and F. J. DiSalvo, Inorg. Chem. **29**, 4059 (1990).

[87] H. Toriumi, G. Kobayashi, T. Saito, T. Kamiyama, T. Sakai, T. Nomura, S. Kitano, H. Habazaki, and Y. Aoki, Chem. Mater. **34**, 7389 (2022).

[88] H. Ubukata, F. Takeiri, K. Shitara, C. Tassel, T. Saito, T. Kamiyama, T. Broux, A. Kuwabara, G. Kobayashi, and H. Kageyama, Sci. Adv. **7**, eabf7883 (2021).

[89] E. Novak, L. Daemen, A. J. Ramirez-Cuesta, Y. Cheng, R. Smith, T. Egami, and N. Jalarvo, Sci Rep **12**, 6194 (2022).

[90] H. Jobic, K. Hahn, J. Kärger, M. Bée, A. Tuel, M. Noack, I. Girnus, and G. J. Kearley, J. Phys. Chem. B **101**, 5834 (1997).

[91] T. Lorne, *Contribution of Inelastic Neutron Scattering to the Characterization of the Grafting of Fluorophores onto Double-Walled Carbon Nanotubes*, Ph.D. thesis, Université Paul Sabatier - Toulouse III (2017).